

Carbon Nano

7. Carbon Nanofibers

Yoong A. Kim, Takuya Hayashi, Morinobu Endo, Mildred S. Dresselhaus

Carbon nanofibers are sp^2 -based linear, noncontinuous filaments that are different from carbon fibers, which are continuous with diameter of several micrometers. This chapter provides a review on the growth, structural properties, and practical applications of carbon nanofibers as compared with those of conventional carbon fibers. Carbon nanofibers can be produced via catalytic chemical vapor deposition (CVD) as well as the combination of electrospinning of organic polymer and thermal treatment. The amount of commercially available carbon nanofiber worldwide is ca. 500 t/year. Carbon nanofibers exhibit high specific area, flexibility, and superstrength due to their nano-sized diameter, which allows them to be used in electrode materials of energy storage devices, hybrid-type filler in carbon-fiber-reinforced plastics, and bone tissue scaffold. It is envisaged that carbon nanofibers will be key materials of green science and technology through a close combination with carbon fibers and carbon nanotubes.

7.1 Similarity and Difference Between Carbon Fibers and Carbon Nanofibers 234

7.1.1 Basic Concepts 234

7.1.2 Synthesis and Properties of Carbon Fibers	235
7.1.3 Vapor-Grown Carbon Fibers	236

7.2 Growth and Structural Modifications of Carbon Nanofibers 238

7.2.1 Catalytically Grown Cup-Stacked Type	238
7.2.2 Catalytically Grown Platelet Type	241
7.2.3 Electrospun Carbon Nanofibers	244
7.2.4 Electrospun Porous Carbon Nanofibers	249

7.3 Applications of Carbon Nanofibers 251

7.3.1 Electrode Material in Lithium-Ion Secondary Batteries	251
7.3.2 Electrode Material for Supercapacitors	253
7.3.3 Supporting Material for Metal Nanoparticles	256
7.3.4 Bone Tissue Scaffold	257

7.4 Conclusions 257

References 258

Carbon nanofibers could be defined as sp^2 -based linear filaments with diameter of ca. 100 nm that are characterized by flexibility and their aspect ratio (above 100). Materials in fiber form are of great practical and scientific importance. The combination of high specific area, flexibility, and high mechanical strength allows nanofibers to be used in our daily life as well as in fabrication of tough composites for vehicle and aerospace applications. However, carbon nanofibers should be distinguished from conventional carbon fibers [7.1–3] and vapor-grown carbon fibers (VGCFs) [7.4–10] in their small diameter (Fig. 7.1).

Conventional carbon fibers and VGCFs have diameters of several micrometers (Fig. 7.1c,d). In addition, carbon nanofibers are different from well-known carbon nanotubes [7.5, 11–14]. Carbon nanofibers can be grown by passing carbon feedstock over nano-sized metal particles at high temperature [7.4–10], which is very similar to the growth conditions for carbon nanotubes. However, their geometry is different from concentric carbon nanotubes containing an entire hollow core, because they can be visualized as consisting of regularly stacked, truncated conical or planar layers along the filament length [7.15–18].

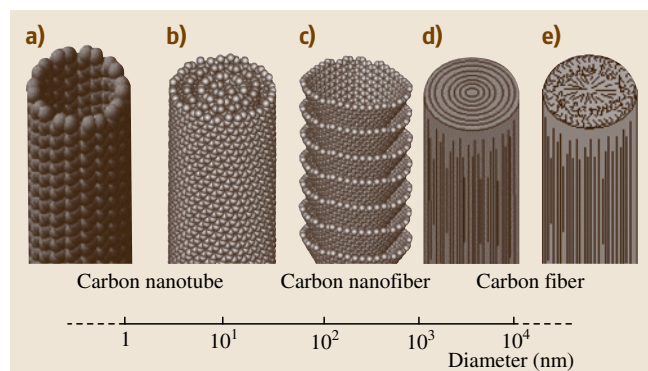


Fig. 7.1 Schematic comparison of the diameter dimensions on a log scale for various types of fibrous carbon materials

This unique structure endows them with semiconducting behavior [7.19] and chemically active end planes on both the inner and outer surfaces of the nanofibers, thereby making them useful as supporting materials for catalysts [7.20], reinforcing fillers in polymeric composites [7.21], hybrid-type fillers in

carbon-fiber-reinforced plastics [7.22–24], and photocurrent generators in photochemical cells [7.25, 26].

Alternatively, carbon nanofibers can be fabricated by the right combination of electrospinning of organic polymers and thermal treatment in an inert atmosphere. The electrospinning technique has been considered to be one of the advanced fiber formation techniques from polymer solution by using electrostatic forces [7.27–30]. Nanofibers produced by electrospinning exhibit noticeably different properties, such as nanosized diameter, high surface area, and thin web morphology, which make them applicable for fabrication of high-performance nanocomposites, tissue scaffolds, and energy storage devices [7.31–37].

Within this context, intensive studies on the synthesis, characterization, and possible applications of carbon nanofibers have been carried out during the last decade. In this chapter, we review their synthesis techniques and interesting textural properties, as well as promising applications of carbon nanofibers that have been developed over the past 10 years.

7.1 Similarity and Difference Between Carbon Fibers and Carbon Nanofibers

Since carbon nanofibers could be considered as a one-dimensional (1-D) form of carbon, their structure and properties are closely related to those of other forms of carbon, especially to crystalline three-dimensional graphite, turbostratic carbons, and to their constituent two-dimensional (2-D) layers. Therefore, several forms of conventional carbon materials should be mentioned in terms of their similarities and differences relative to carbon nanofibers. Especially, direct comparison should be made between fibrous carbon materials, because carbon fibers act as a bridge between carbon nanofibers and conventional bulk carbon materials. In this section, the structures of carbon fibers as well as VGCFs are described, with strong emphasis on the similarities and differences of these 1-D carbon materials.

7.1.1 Basic Concepts

Carbon fibers represent an important class of graphite-related materials that are closely related to carbon nanofibers with regard to structure and properties. Carbon fibers have been studied scientifically since the late 1950s, and fabricated industrially since 1963. They

are now becoming a technologically and commercially important material in aerospace, construction, sports, electronic device, and automobile industries. The global carbon fiber market has now grown to about 12 500 t/year of product, after 40 years of continuous research and development (R&D) work [7.1–3]. Carbon fibers are defined as a filamentary form of carbon with an aspect ratio (length/diameter) greater than 100. Probably, the earliest documented carbon fibers are the bamboo-char filaments made by Edison for use in the first incandescent light bulb in 1880. With time, carbon fibers were replaced by more robust tungsten filaments in light bulb applications, and consequently carbon fiber R&D vanished at that early time. However, in the late 1950s, carbon fibers once again became important because of the aggressive demand from the aerospace industry for lightweight, strong composite materials, in which carbon fibers are used as a reinforcement agent in conjunction with plastics, metals, ceramics, and bulk carbon materials. The specific strength (strength/weight) and specific modulus (stiffness/weight) of carbon-fiber-reinforced composites explain their importance as engineering materials,

due to the high performance of their carbon fiber constituents.

Since the temperature and pressure necessary to prepare a carbon fiber from the liquid phase is at the triple point ($T = 4100\text{ K}$, $p = 123\text{ kbar}$), it would be almost impossible to prepare carbon fibers from the melt under industrial processing conditions. Carbon fibers are therefore prepared from organic precursors. This preparation is generally done in three steps, including stabilization of a precursor fiber in air (at $\approx 300^\circ\text{C}$), carbonization at $\approx 1100^\circ\text{C}$, and subsequent graphitization (at $> 2500^\circ\text{C}$). Fibers undergoing only the first two steps are commonly called *carbon fibers*, while fibers undergoing all three steps are called *graphite fibers*. Carbon fibers are generally used for their high strength, while graphite fibers are used for their high modulus. Historically, Bacon's graphite whisker (Fig. 7.2) has demonstrated the highest mechanical properties of a carbon fiber (with regard to both strength and modulus), comparable to the ideal value for a graphite network [7.38]. Graphitic whiskers were grown under conditions near the triple point of graphite. Then, a structural model was proposed in which layers consisting of graphene sheets are wound around the axis as if rolling up a carpet. These whiskers were used as the performance target in the early stages of carbon-fiber technology, even though they have never been produced on a large scale.

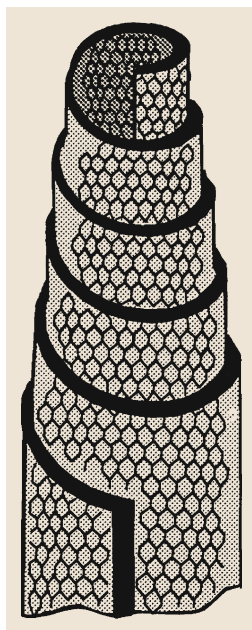


Fig. 7.2 Model for graphite whiskers grown by direct-current (DC) arc discharge of graphite electrodes. Whiskers were reported to have a carpet-rolling structure of graphite sheets with high mechanical strength and modulus along the fiber axis, similar to the ideal values of a graphene sheet

7.1.2 Synthesis and Properties of Carbon Fibers

Scanning electron microscopy (SEM) images together with schematic structural models are shown in Fig. 7.3 for typical carbon fibers: a high-strength polyacrylonitrile (PAN)-based fiber (Fig. 7.3a), a high-modulus PAN-based fiber (Fig. 7.3b), and a mesophase pitch-based carbon fiber (MPCF) (Fig. 7.3c) [7.38, 39]. The PAN-based fibers consist of small sp^2 -carbon structural units preferentially aligned with the carbon hexagonal segments parallel to the fiber axis. This orientation is responsible for the high tensile strength of PAN-based carbon fibers [7.40]. By varying the processing conditions (e.g., oxidation conditions, choice of precursor material, and especially by increasing the heat treatment temperature) of PAN fibers, better alignment of the graphene layers can be achieved (structural model of Fig. 7.3b), thus leading to stiffer, higher-modulus PAN fibers, but with lower strength [7.39]. PAN-based fibers are one of the typical hard carbons. MPCFs consist of well-aligned graphitic layers arranged nearly parallel to the fiber axis, and this high degree of preferred orientation is responsible for their high modulus or stiffness as well as their relatively high graphitizability. The structures described above give rise to different physical properties, although each type of fiber features hexagonal carbon networks, possessing the strongest covalent bonds in nature (C–C bonds). These strong interatomic bonds lie in sheets essentially parallel to the fiber axis and are responsible for the high mechanical performance of these carbon fibers.

Referring to Fig. 7.4a, we see that PAN-based fibers have high strength and MPCFs have high modulus, while VGCFs provide mainly ultrahigh-modulus materials [7.4, 41]. In this figure we also observe isotropic pitch-based (general grade) fibers, exhibiting much lower modulus and strength, but widely used in composites with cement matrix for construction due to their low cost and high chemical stability. Figure 7.4b demonstrates a direct indication of the differences in the mechanical properties of various carbon fibers, from low-modulus high-strength to high-modulus low-strength fibers, from the lower left to the upper right in the photograph, where a yarn containing 500 fibers was initially placed in a horizontal position. These fibers are combined with other materials in order to design suitable mechanical properties, and the fibers are used as a filler for various advanced composite materials. To obtain high performance in carbon and graphite fibers, it is very important to control the

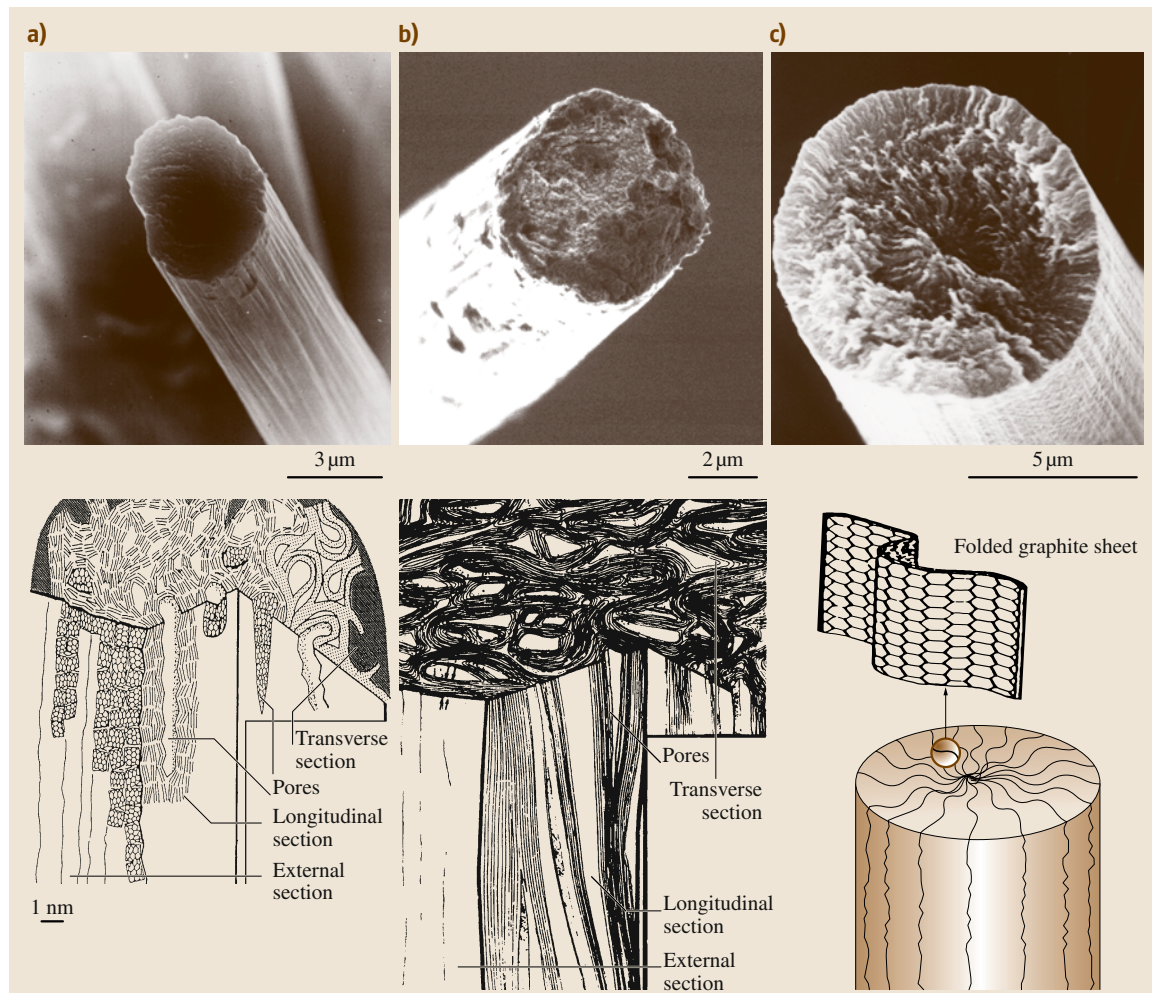


Fig. 7.3a–c SEM micrographs of three types of carbon fibers and corresponding structural models: **(a)** high-strength PAN-based fiber, **(b)** high-modulus PAN-based fiber, and **(c)** a mesophase pitch-based fiber. In the second row, for each fiber type, a schematic diagram of the fiber structure is shown

microstructure and nanostructure by selecting the appropriate organic precursor as well as the processing conditions.

7.1.3 Vapor-Grown Carbon Fibers

VGCFs have a very special structure like annular rings on a tree (Fig. 7.5a) and are synthesized by a somewhat different formation process than that used to produce PAN-based and MPCFs. In particular, VGCFs are not prepared from a fibrous precursor, but rather from hydrocarbon gas, using a catalytic growth process outlined in Fig. 7.5b [7.5–10]. Ultrafine transition-metal par-

ticles, such as iron particles with diameter less than 10 nm, are dispersed on a ceramic substrate, and a hydrocarbon, such as benzene diluted with hydrogen gas, is introduced at temperatures of about 1100 °C. Hydrocarbon decomposition takes place on the catalytic particle, leading to continuous carbon uptake by the catalytic particle and continuous output by the particle of well-organized tubular filaments of hexagonal sp^2 carbon. The rapid growth rate of several tens of $\mu\text{m}/\text{min}$, which is 106 times faster than that observed for the growth of common metal whiskers [7.37], enables production of commercially viable quantities of VGCFs. Evidence in support of this growth model is provided

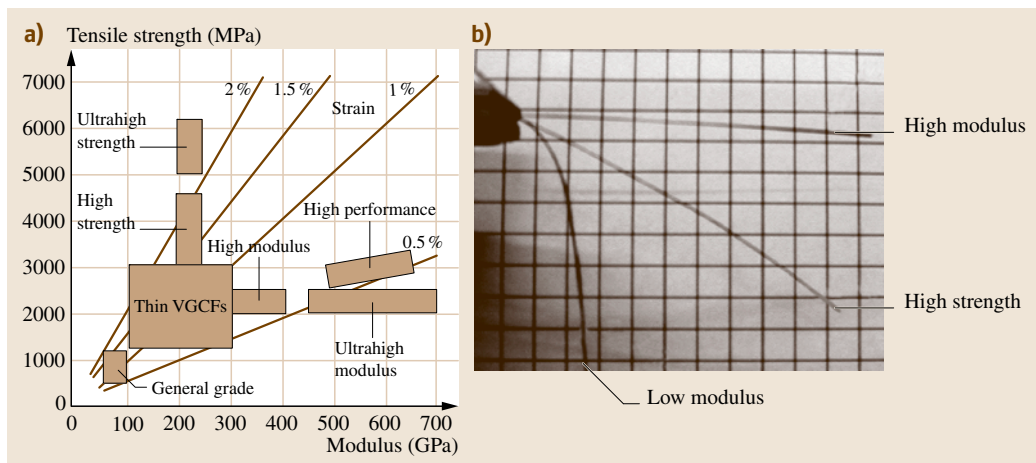


Fig. 7.4 (a) Mechanical properties of various kinds of carbon and graphite fibers, and (b) direct comparison of the mechanical properties for high-strength and high-modulus fibers. A low-modulus fiber droops under its own weight, whereas high-modulus fibers do not

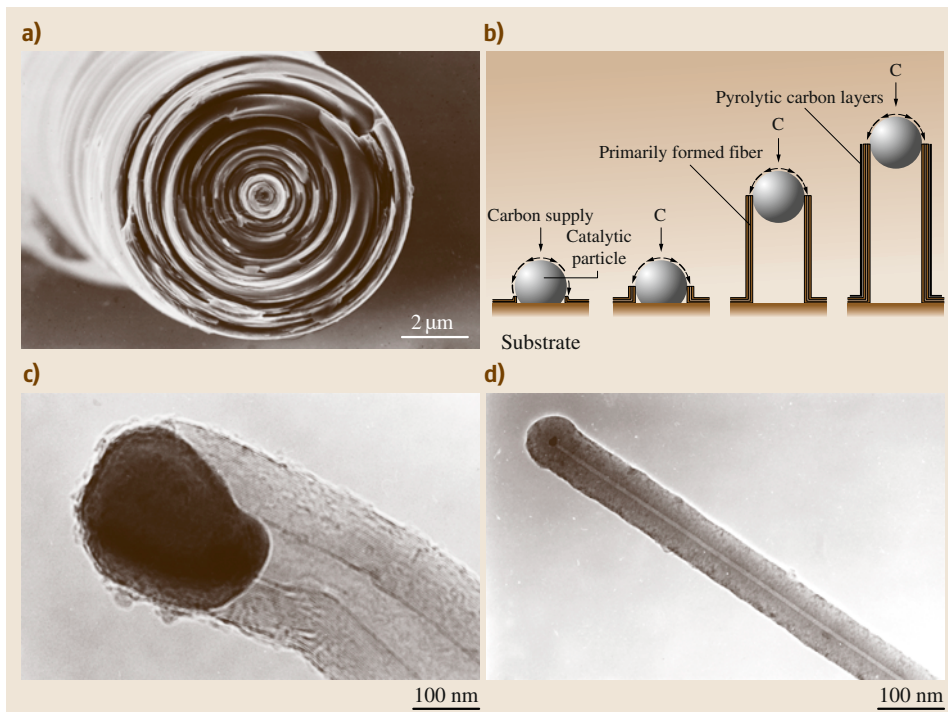


Fig. 7.5 (a) SEM image of vapor-grown carbon fibers, (b) suggested growth mechanism of VGCFs using ultrafine catalytic metal particles, (c) very early stage of tubule growth in which the catalytic particle is still active, promoting elongation. The primary tubule thus formed acts as a core for vapor-grown fibers. (d) The fiber is obtained through a thickening process, such as pyrolytic deposition of carbon layers on the primary tubule. The encapsulated catalytic particle can be seen at the tip of the hollow core

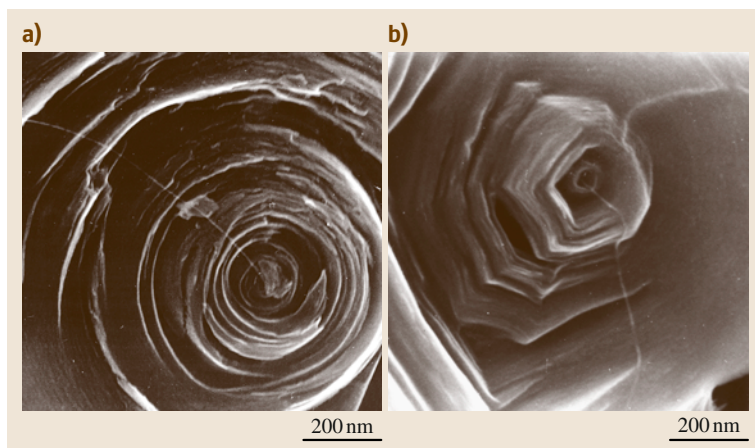


Fig. 7.6 (a) Carbon nanotube exposed at the broken end of a vapor-grown carbon fiber: (a) as grown, and (b) heat-treated at 3000 °C. The sample is fractured by pulverization, and the core diameter is ≈ 5 nm. These images suggest a structural discontinuity between the nanotube core of the fiber and the CVD-deposited carbon layers, and also show the strong mechanical properties of the nanotube core, which maintains its form after breakage

by the presence of catalytic particles at the tips of the resulting VGCFs (Fig. 7.5c) [7.38]. The primary hollow tubule is first formed by the catalytic process (with a diameter of less than several nanometers), and the tubule is then thickened by a successive chemical vapor deposition (CVD) process, corresponding to deposition of pyrolytic carbon layers on the primary tubular core (Fig. 7.5d).

Interestingly, at the center of the annular ring structure, we can clearly observe an extruded carbon

nanotube (with diameter ≈ 5 nm) (Fig. 7.6a), which serves as a template for growing the thicker carbon fiber [7.42]. This tubular core implies a discontinuity in the structure between the core and the thickened periphery of the carbon fiber. Such a discontinuity in the structure is retained even after heat treatment at temperatures as high as 3000 °C. This graphitization process introduces a fully developed graphite structure in the peripheral region of a VGCF, exhibiting a polygonal shape (Fig. 7.6b).

7.2 Growth and Structural Modifications of Carbon Nanofibers

This section presents how carbon nanofibers are fabricated, and their morphological and physicochemical modifications by post treatments are presented in relation to their microstructure. We give an overview of two different synthetic methods: the catalytic chemical vapor deposition method, and the combination of electrospinning with subsequent thermal treatment.

7.2.1 Catalytically Grown Cup-Stacked Type

A catalytic thermal chemical vapor deposition synthesis method has been extensively investigated as a promising method for large-scale production of carbon nanotubes and carbon nanofibers [7.43–45]. Through precise control of the synthesis conditions, it is possible to tailor the diameter, crystallinity, and also orientation of the cone angle with respect to the fiber axis [7.46–48]. Carbon nanofibers with a large hollow core and a large portion of open edges at the outer surface and also in the inner channels, due to the truncated graphene cone morphol-

ogy (cup-stacked), are characterized in terms of their microstructure, oxidation behavior, and also graphitizability, and are compared with those of conventional tubular types of carbon nanofibers. These structural characteristics as well as their potential low production cost using a floating reactant production system may make it possible to use such carbon nanofibers in the fabrication of absorbent materials, catalyst supports, field emitters, gas storage components, and composite materials.

Field-emission scanning electron microscopy (FE-SEM) and transmission electron microscopy (TEM) images at low magnification (Fig. 7.7a,b) reveal relatively long and straight carbon nanofibers with a hollow core along the fiber length (Fig. 7.7c), which exhibit diameters ranging from 50 to 150 nm and lengths up to 200 μm . One of the main characteristics of these fibers is a large hollow core, as compared with conventional tubular-type nanofibers. In addition, we can find some differences in the ratio of the outer

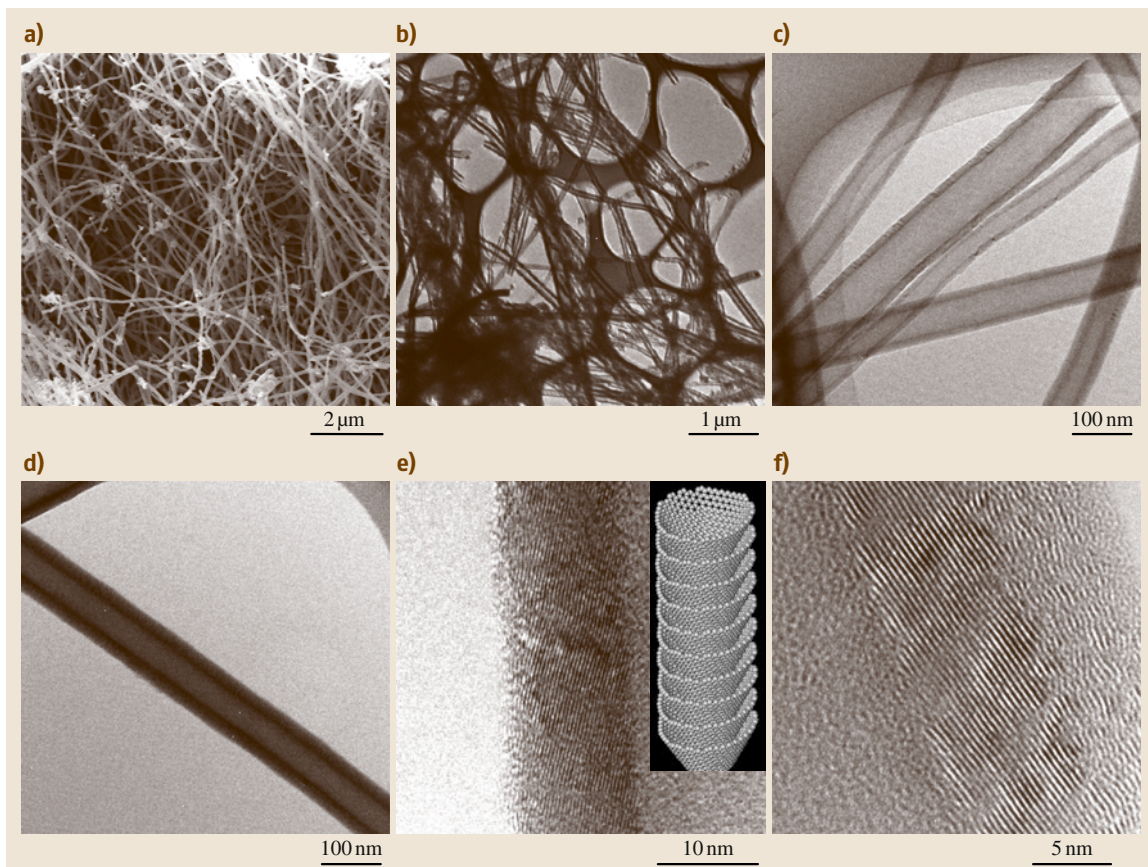


Fig. 7.7 (a) FE-SEM image of nanofibers showing a long and straight morphology; (b) TEM image of nanofibers with a hollow core at low resolution; (c) TEM image of uncoated nanofibers with a large hollow core; (d) TEM image of coated nanofibers with a large hollow core; (e) HRTEM image of an uncoated nanofiber (*inset* shows a schematic model of a carbon nanofiber); (f) HRTEM image of a coated nanofiber

diameter to the inner diameter, i.e., the wall thickness of the carbon nanofibers, as shown in the TEM images of Fig. 7.7c,d. To study these differences in detail, high-resolution TEM (HRTEM) studies have been carried out for these two types of samples. One type of nanofiber shows a truncated cone microstructure (Fig. 7.7e), whereas the other type of nanofiber contains a certain portion of amorphous carbon (coated structure) (Fig. 7.7f). The truncated cone angle (cup) with regard to the fiber axis, measured by electron diffraction (ED), taking the fast Fourier transform (FFT) of several TEM images, lies mainly between 45° and 80° . The observation of (110) planes of graphite might be due to a superposition of conical graphene sheets with ABAB stacking. In terms of the growth mechanism, uncoated nanofibers (Fig. 7.7e), consisting of stacked conical

graphene sheets, are primarily formed by catalytic effects, while the outer part of the coated nanofiber (Fig. 7.7f) corresponds to amorphous carbon deposited during the secondary thickening growth process.

To understand the unique properties of these novel nanofibers, such as a large hollow core and a conical morphology, it is indispensable to mention the morphology of the catalytic metal particles used in the growth process. It has been clearly shown that the microstructure of the nanofibers is determined by the shape of the metal particle at the tip of the fiber (Fig. 7.8a,b). Carbon derived from the decomposition of hydrocarbons dissolved in the metal particle might precipitate as graphitic carbon. This carbon replication from metal particles results in the formation of stacked truncated cones, which grow graphitic nanofibers [7.48]. Along

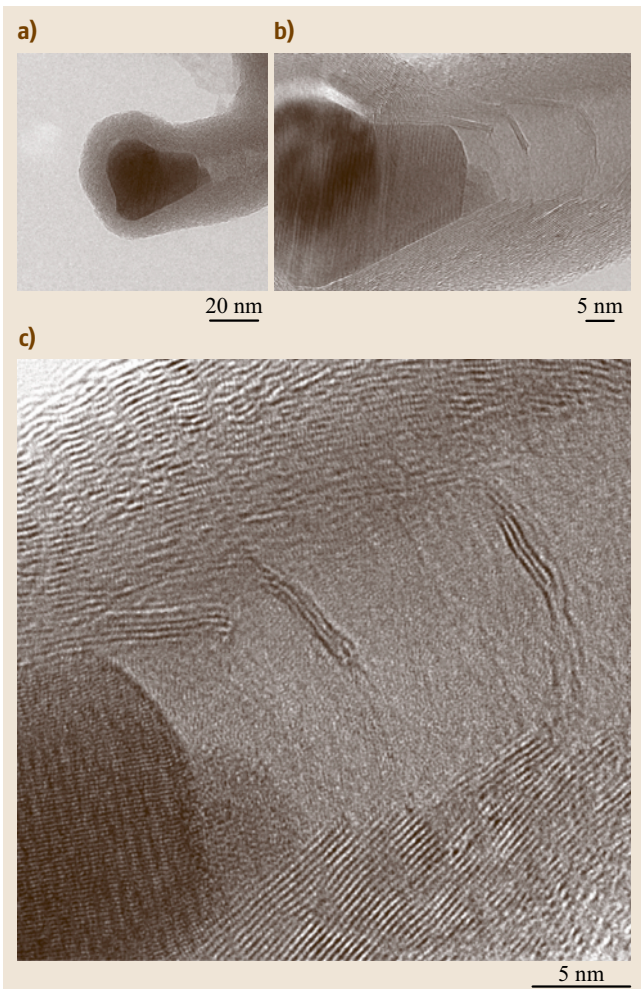


Fig. 7.8 (a) HRTEM image of a typical metal particle at the tip of the nanofibers; (b) and (c) enlarged HRTEM images. (Note that the truncated conical graphene sheets replicate the shape of the rear part of the metal particle)

the fiber axis (Fig. 7.8c), there are some disordered and wavy regions, which might be due to the relaxation of carbon layers as a result of cooling [7.49]. Based on this study, it is possible to say that the size of the metal particle in the growth direction of the fiber is directly related to the size of the hollow core, which is also determined by the composition of the catalytic particle, the type of carbon feedstock, and the reaction temperature.

The outer and also inner surfaces of the nanofiber have to be covered entirely by open edges, i.e., the end face of the graphitic conical sheets from the point of view of the growth mechanism. Practically, the deposi-

tion of amorphous carbon on the catalytically induced graphitic carbon phase, which is unavoidable in the synthetic process of nanofibers, and also the possible formation of loops between adjacent conical graphene sheets might deteriorate the total chemical and physical reactivity of the nanofibers. To solve this problem, an air oxidation process is applied to prepare nanofibers with an increased fraction of open edge sites. Figure 7.9a shows Raman spectra for oxidized uncoated nanofibers (Fig. 7.7c,e) at different temperatures. Modification of the surface of the nanofiber starts at 520 °C, and then the optimal oxidation temperature is found to be at 530 °C for our experimental conditions, based on a decreased half-width at half-maximum (HWHM) and intensity of the D peak at 1355 cm⁻¹ (the defect mode), the appearance of a shoulder peak at 1620 cm⁻¹, and also a decreased relative intensity (I_D/I_G). When oxidized at 540 °C, structural disruption might occur, due to severe oxidation, based on an increased intensity of the D peak and also a large value of the relative intensity ($I_D/I_G = 0.9674$). For the case of an optimally modified sample (530 °C), consistent fiber morphology (Fig. 7.9b) and a somewhat decreased wall thickness (Fig. 7.9c) are observed, accompanying an increase in the specific surface area from 49.67 to 146.47 m²/g.

The graphitization process is known as one of the most efficient ways to modify the microstructure of carbons [7.50, 51]. TEM images of graphitized nanofibers are shown in Fig. 7.10. The most interesting change caused by the graphitization process is a morphological transformation from a smooth-walled tubule type to a reversing sawtooth type with regular pitch (Fig. 7.10a,b,d). The other features of the graphitized nanofibers are the formation of long links along the outer and inner sides of the fibers at regular pitch intervals (closure of open cups on both sides) and loop formation between neighboring conical sheets (Fig. 7.10c,e), resulting in the formation of triangle-type nanomaterials (Fig. 7.10f). Also, the morphologies of the graphitized samples are strongly affected by the microstructure of the starting materials (Fig. 7.10b from an uncoated nanofiber and Fig. 7.10d from a coated nanofiber). For the graphitization mechanism, the decrease in interlayer spacing [from 3.45 to 3.395 Å, based on x-ray diffraction (XRD) analysis] is smaller than that of CVD-based carbon materials. In fact, the number of loops increases with increasing heat treatment temperature. Therefore, the formation of loops in both the inner and outer surfaces of the nanofiber might retard the three-dimensional stacking ordering caused by mass transformation, and also give indirect evidence

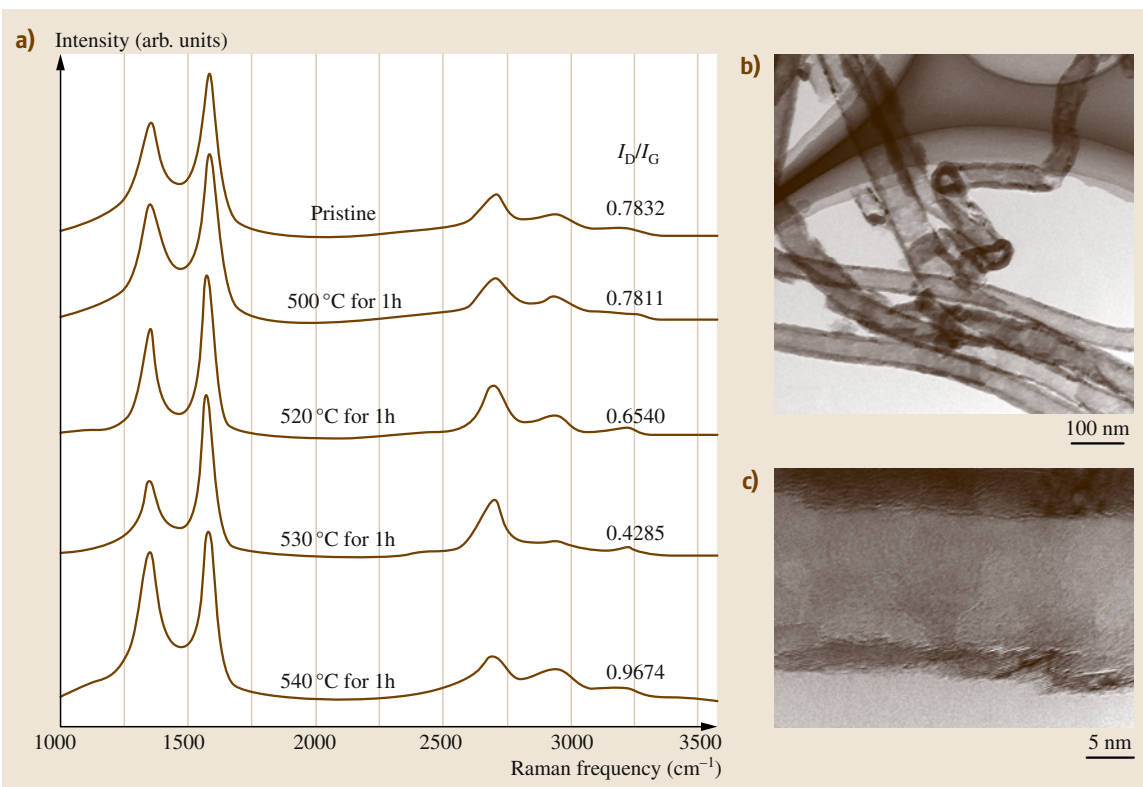


Fig. 7.9 (a) Raman spectra of nanofibers oxidized at different temperatures in air atmosphere for 1 h (I_D/I_G is the relative intensity ratio of the G peak over the D peak). (b) TEM image of nanofiber morphology for experimental condition at 530 °C, (c) high resolution TEM image of nanofiber showing decrease in wall thickness, and an increase in specific surface area

for the carbonization and graphitization mechanism of hard carbon materials.

7.2.2 Catalytically Grown Platelet Type

SEM and TEM studies reveal that carbon nanofibers have the form of short rods (Fig. 7.11a) with semirectangular cross-sectional morphology (inset to Fig. 7.11a). Moreover, crystalline graphene layers are stacked regularly along the length direction of the carbon nanofiber (Fig. 7.11b), the accessible surface area of which is fully covered with chemically active end planes. When an undoped sample was thermally treated in argon at 2200 °C and 2500 °C, the active edges were structurally converted to energetically stable multiloops (Fig. 7.11c). For the undoped sample, multiloop formation was not clearly observed at 1900 °C. In contrast, we clearly observed formation of multiloops in a boron-doped sample treated at 1900 °C. In addition, the B-doped sample

treated at 2500 °C (Fig. 7.11f) had a higher number of multiloops than did the corresponding undoped sample (Fig. 7.11d). Therefore, we assume that B atoms play an important role in loop formation, leading to changes in the surface morphology of carbon nanofibers during high-temperature thermal treatment.

We carried out x-ray diffraction (Fig. 7.12a,b) and Raman spectroscopy (Fig. 7.12c,d) studies to investigate the changes in the structure of carbon nanofibers that result from high-temperature thermal treatment in the presence of B atoms. The sharp (002) line for the as-grown sample indicates the relatively high crystallinity of the catalytically grown carbon nanofibers (Fig. 7.12a). As the heat treatment temperature is increased for the undoped sample, the (002) line shifts to higher angles. The decreased HWHM of the D band (defect-induced mode) at 1350 cm^{-1} and the G band (E_{2g} graphitic mode) at 1580 cm^{-1} , as well as decreased R value (intensity of the D band/intensity of

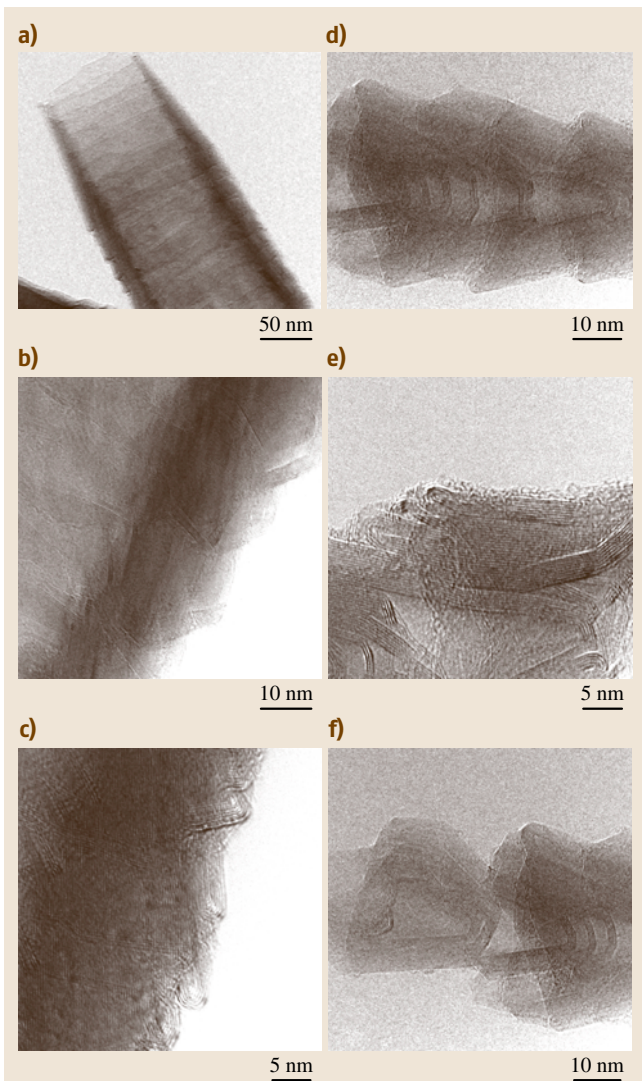


Fig. 7.10 (a), (b), (c) HRTEM images of a graphitized uncoated nanofiber [starting material is uncoated nanofiber (Fig. 7.1c,e)]; (d), (e), (f) HRTEM images of a graphitized coated nanofiber

the G band) in the Raman spectra (Fig. 7.12c and Table 7.1) indicate that the structure of the undoped carbon nanofibers was improved by the high-temperature thermal treatment. Even though the undoped nanofibers were thermally treated at 2500 °C in argon, there was no splitting of the (101) and (100) lines in the x-ray diffraction patterns; furthermore, no distinctive reduction in the intensity of the D band was observed in the Raman spectrum for the undoped sample. This result

can be explained by the formation of stable multiloops on the outer surface of the carbon nanofibers (TEM images in Fig. 7.11), which effectively inhibited three-dimensional stacking [7.52]. In the case of B-doped carbon nanofibers, we observed highly improved structures upon thermal treatment at high temperatures (Fig. 7.12b, and lower value of interlayer spacing in Table 7.1), reflecting the fact that B atoms are graphitization accelerators in carbon materials. Recently, it was reported that resonance Raman spectroscopy is extremely sensitive to the end planes in graphitic nanoribbons [7.53]. It is well known that the Raman line at 1620 cm^{-1} in the as-grown sample originates from the end planes in carbon materials [7.54]. With increasing thermal treatment temperature, the Raman line at 1620 cm^{-1} disappears, which is consistent with the formation of energetically stable multiloops at the end planes. However, the high intensity of the D and D' bands as well as the high R values observed for B-doped samples (Fig. 7.12d) strongly indicate that the B atoms were incorporated into the sp^2 carbon network via substitution for carbon, because the B–C distance is slightly larger than the C–C distance [7.55]. Notably, the higher value of the HWHM of the G band (Table 7.1) (which is intrinsically related to phonon lifetime) indicates that the B atoms incorporated into the carbon network create optical defects. In addition, we have confirmed the presence of substitutional incorporation of B into carbon fibers by using x-ray photoelectron spectroscopy.

To evaluate the physical changes in the B-doped carbon nanofibers, we measured their electrical resistivity in the bulk state using a four-point probe method (Fig. 7.13a). After pouring a specific amount of the carbon nanofibers into the sample holder, we measured the volumetric resistivity at a nanotube mass density of 1.23 g/cm^3 . Generally, B-doped samples exhibited improved electrical conductivity compared with undoped samples. It is noteworthy that the electrical resistivity in the bulk state is determined by both the contact resistivity between fibers and the intrinsic resistivity of individual fibers. Therefore, we measured the electrical resistivity of a freestanding individual nanofiber using methods described in the relevant literature [7.56, 57]. After spin-coating a nanofiber suspension onto Au/Ti electrodes, we confirmed using FE-SEM that an individual fiber had bridged the electrode gap (500 nm). We then obtained the intrinsic resistivity of an individual nanofiber from a linear current–voltage relation up to 1 V. As shown in Fig. 7.13b, the electrical resistivity at room temperature of the individual as-grown

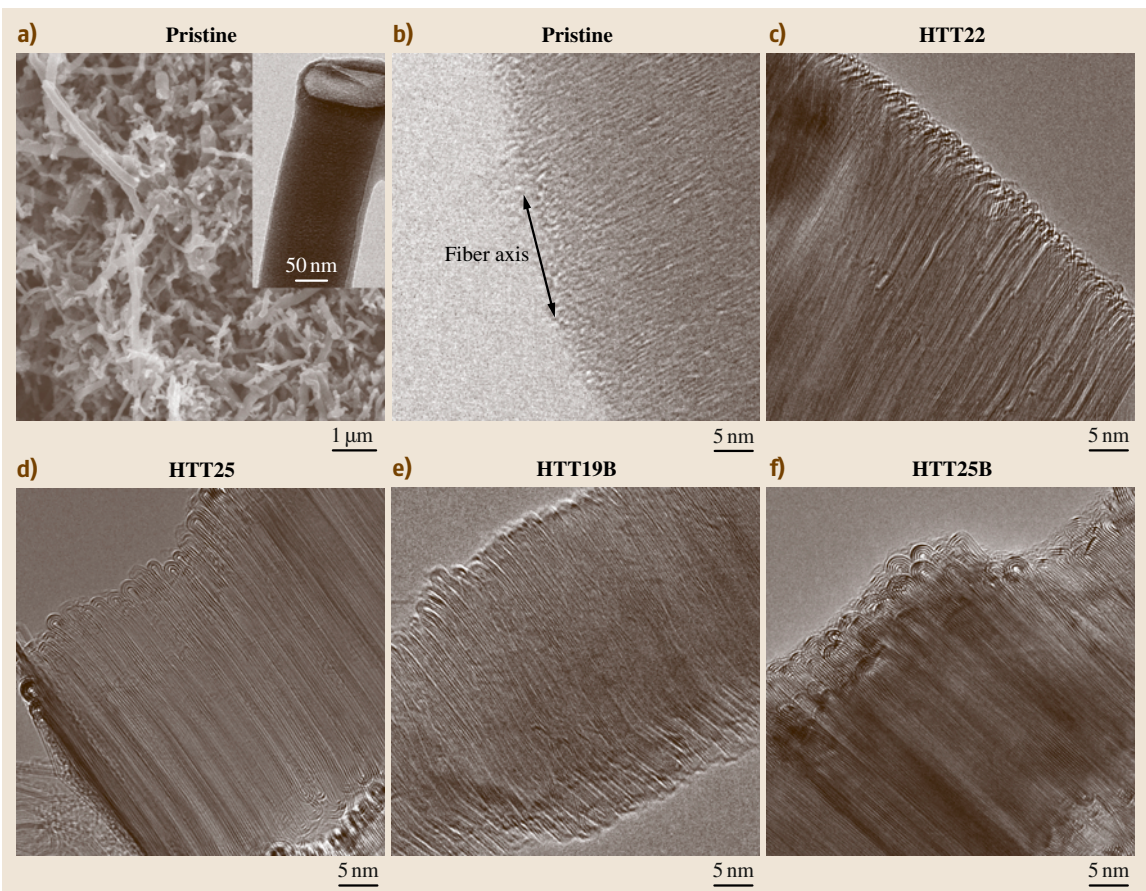


Fig. 7.11 (a) SEM and (b) TEM images of as-grown platelet-type carbon nanofibers. *Inset* shows the semirectangular cross-sectional morphology of the carbon nanofibers. Note that the crystalline graphene layers are stacked regularly along the length of the carbon nanofiber, the accessible surface area of which is covered with active edges. TEM images of samples thermally treated at (c) 2200 °C and (d) 2500 °C without B, and at (e) 1900 °C and (f) 2500 °C in the presence of B

carbon nanofiber was extremely high ($\approx 280 \text{ k}\Omega$) compared with an arc-based multi-walled carbon nanotube ($\approx 2.4 \text{ k}\Omega$) [7.58]. This result can be explained by the peculiar platelet-like morphology of the nanofibers investigated in the present study: the current flow between graphene layers in graphite (along the fiber length direction) is six times lower than that in the graphene plane (a -axis) [7.59]. Although no general relationship between thermal treatment temperature and the electrical resistivity of an individual fiber was observed (possibly due to the inhomogeneous diameter distribution), we confirmed that the substituted B atoms in the carbon nanofibers lowered the Fermi level, thus increasing the electrical conductivity of the carbon nanofibers.

In addition, we evaluated the effectiveness of the B-doped carbon nanofibers as an anode material for high-rate lithium-ion batteries (LIBs). We demonstrated that the substituted B atoms improve the electrical conductivity as well as give rise to multiloop formation, producing an outer surface that is stable against (or inert to) electrolytes. Figure 7.14a,b shows the voltage profiles of the second discharging/charging cycle for carbon nanofibers prepared under different conditions. The increased proportion of the lithium discharge/charge plateau below 0.2 V with increasing thermal treatment temperature (Fig. 7.14a) and B doping (Fig. 7.14b) indicates that Li insertion/desertion was the main mechanism and that the structural

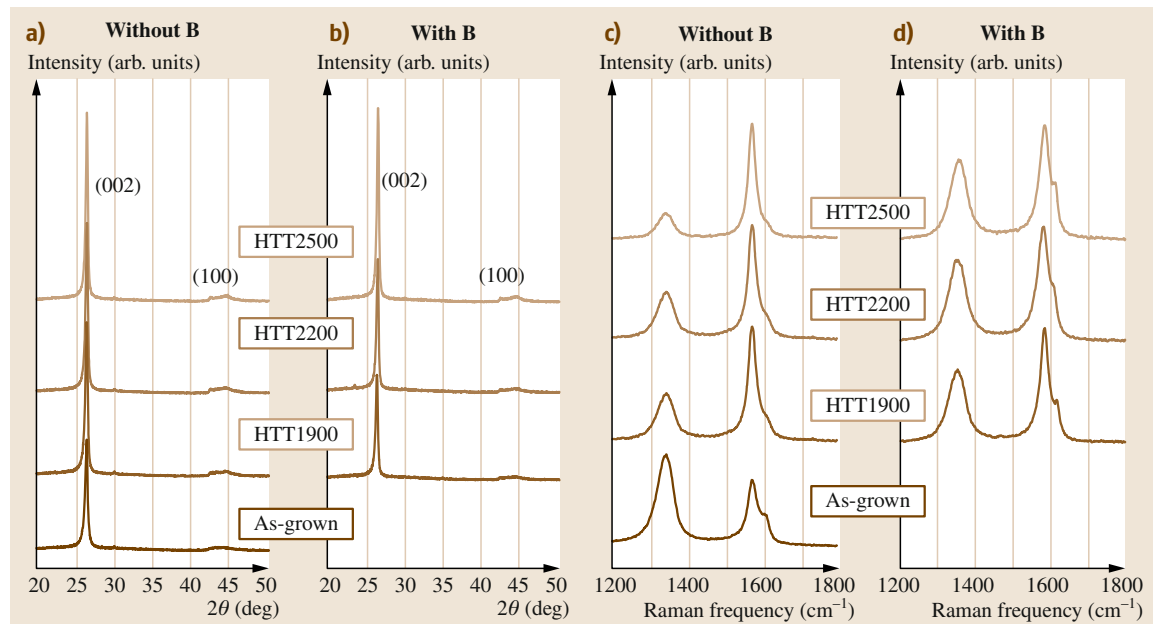


Fig. 7.12a–d X-ray diffraction patterns of carbon nanofibers: **(a)** without boron, and **(b)** with boron; Raman spectra of carbon nanofibers: **(c)** without boron, and **(d)** with boron. From bottom to top, results are shown for the as-grown sample and samples thermally treated at 1900 °C, 2200 °C, and 2500 °C

Table 7.1 Raman and crystallographic factors of undoped and boron-doped platelet-type carbon nanofibers

	FWHM of the G band (cm^{-1})	R value ^{a)}	2θ (°)	d_{002} (nm) ^{b)}	L_c (nm) ^{b)}
Pristine	34.97	1.390	26.430	3.369	18.02
HTT1900	30.97	0.417	26.498	3.361	21.51
HTT2200	25.43	0.250	26.520	3.358	24.20
HTT2500	24.72	0.241	26.528	3.357	25.31
HTT1900B	31.25	0.654	26.458	3.366	24.67
HTT2200B	36.15	0.724	26.523	3.353	28.74
HTT2500B	36.08	0.705	26.566	3.352	29.82

^{a)} R value is the intensity of the D band divided by the intensity of the G band,

^{b)} d_{002} and L_c are obtained using the Scherrer's formula

integrity was improved. The large amount of Li adsorption onto B-substituted planar carbon materials has been theoretically confirmed by molecular-orbital calculations [7.60]; this improved Li adsorption is one reason for the improved discharge capacity of the B-doped carbon nanofibers, since B atoms act as an electron acceptor and induce redistribution of the π -electrons within loops. In addition, we found that the capacity of the B-doped carbon nanofibers degraded to a lesser extent at high discharge current density (Fig. 7.14c,d) compared with undoped samples. In other words, substituted B atoms within car-

bon nanofibers enhanced the electrical conductivity of individual carbon nanofibers as well as forming loop-ended surfaces that were stable against (or inert to) electrolytes.

7.2.3 Electrospun Carbon Nanofibers

Polyacrylonitrile (PAN) polymer in dimethylformamide (DMF) can be easily transformed into white-colored nanofiber web using our electrospinning conditions (Fig. 7.15a), because PAN has been widely used as a precursor for conventional carbon fibers. The con-

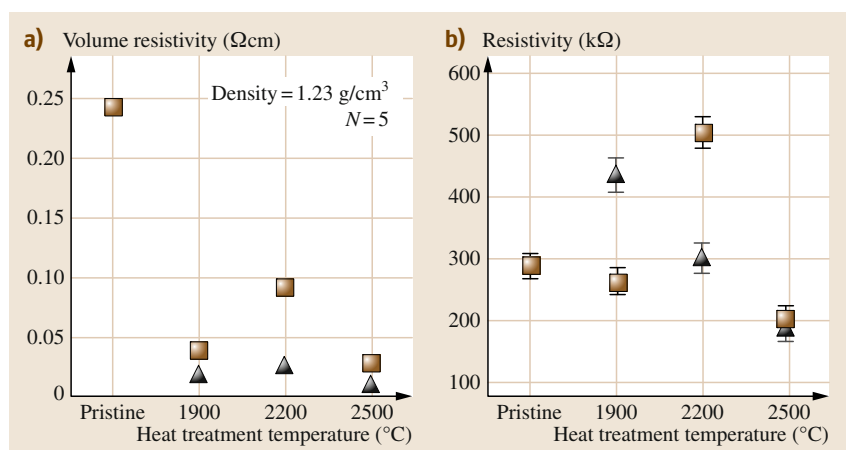


Fig. 7.13 (a) Variations in volumetric resistivity of carbon nanofibers at density of $1.23 \text{ g}/\text{cm}^3$, and (b) electrical resistivity of an individual carbon nanofiber; rectangles denote as-grown and thermally treated undoped carbon nanofibers, while triangles denote boron-doped carbon nanofibers

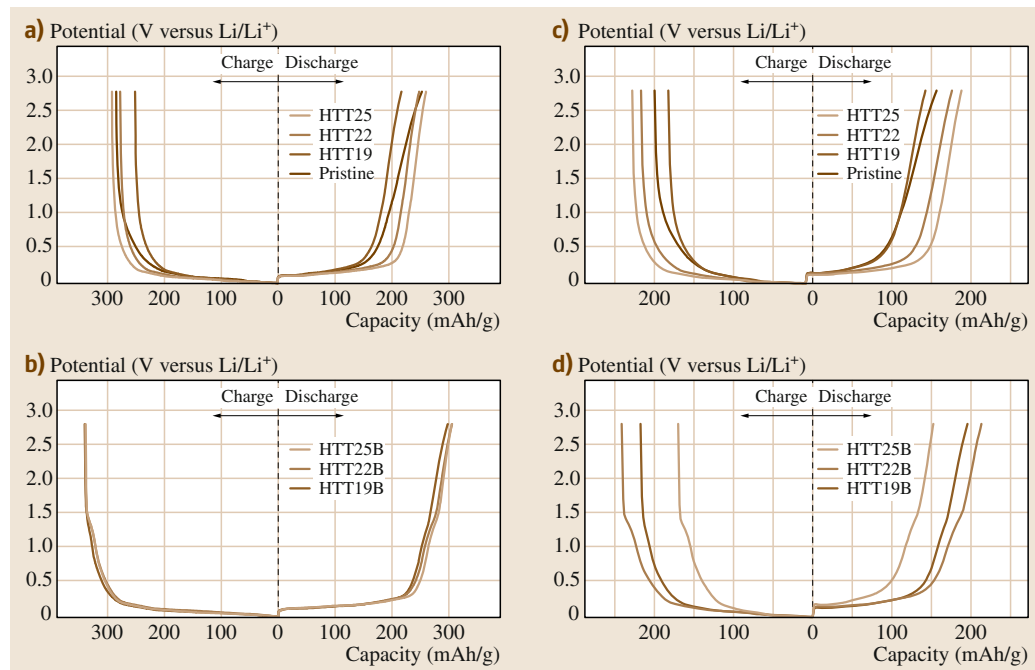


Fig. 7.14a–d Change in potential profile during the second discharging/charging cycle in the range of 0–2.8 V for current densities of (a,b) 30 and (c,d) 100 mA/g

version of a PAN nanofiber to a carbon nanofiber involves stabilization and carbonization. Air stabilization of electrospun nanofiber ($\approx 280^{\circ}\text{C}$ for 1 h under controlled air circulation) is accompanied by a change in color from white to reddish brown (Fig. 7.15b). Finally, when an air-stabilized nanofiber web was thermally treated at 1000°C in an inert atmosphere (e.g., argon or nitrogen gas), the obtained black-colored car-

bon nanofiber web (Fig. 7.15c) exhibited a relatively high carbon yield (up to 40–50%). This oxidative stabilization is considered to be due to the introduction of thermosetting properties to the spun organic fibers, and involves oxygen uptake and subsequent complex chemical and physical reactions occurring on multiple time and temperature scales [7.61, 62]. Thus, the accessible surface area of a precursor will be the determining

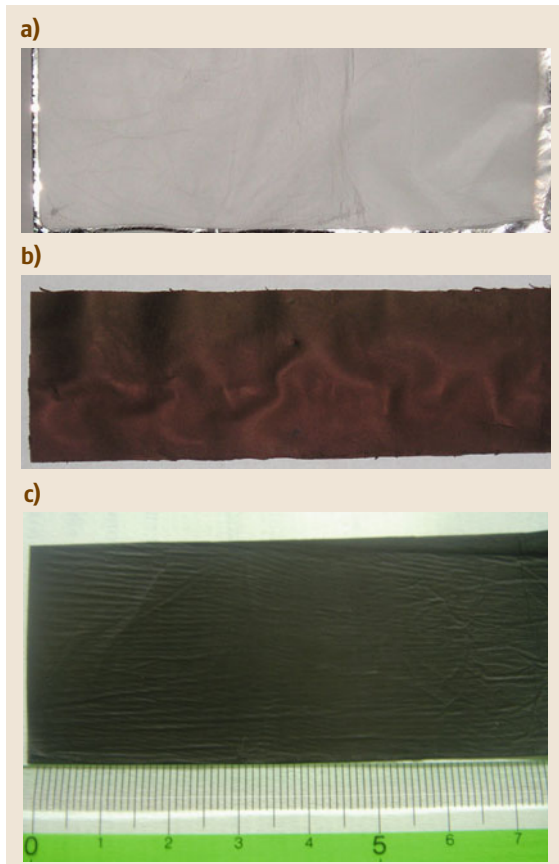


Fig. 7.15a–c Photographs of PAN-derived (a) electrospun nanofiber web (*light-gray color*), (b) air-stabilized web (*dark-brown color*), and web thermally treated at 700 °C (*black color*). It is noteworthy that air stabilization is a critical step for obtaining dimensional stability of nanofibers

factor in terms of the chemical kinetics. To understand the oxidation behaviors in detail, differential thermal analysis was carried out for both micro-sized and nano-sized fibers in air atmosphere (Fig. 7.16). Both samples exhibited single exothermic peaks at around 320 °C, corresponding to oxygen uptake and the subsequent complex chemical reactions [7.61, 62]. The relatively sharp peak for the electrospun sample indicates that the oxygen-induced chemical reactions in nano-sized fibers occur quickly at a specific temperature, as expected. Therefore, the theoretically twofold higher accessible surface area (as derived from the nano-sized diameters) as compared with the micro-sized fibers ($\approx 10 \mu\text{m}$) is quite favorable in decreasing the air stabilization time by a factor of two, because oxygen is believed to dif-

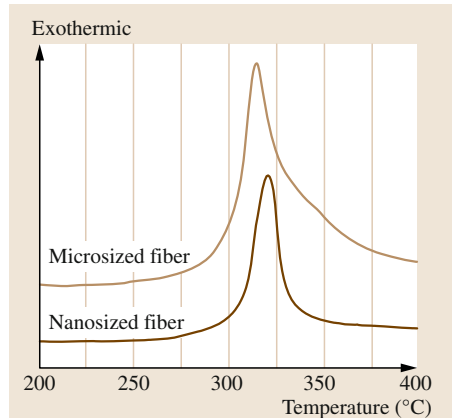


Fig. 7.16 Differential thermal analysis graphs of micro-sized and nano-sized fibers in air atmosphere, respectively (heating rate 10 °C/min)

fuse from the outer surface of fibers kinetically. For our experimental conditions, optimally air-stabilized nanofiber was *flameproof* when the oxygen content was 8–10%.

FE-SEM images of electrospun PAN nanofibers (Fig. 7.17a,b) exhibit a very long and straight fibrous morphology with uniform diameters ranging from 200 to 300 nm (average 250 nm). In addition, nanofibers are partially aligned along the winding direction. When thermally treated at 700 °C, morphological changes from straight to undulated fibers (Fig. 7.17c,d) are caused by large weight loss (up to 30–40%) accompanied by gas evolution (e.g., CO, CO₂, H₂O etc.). For thermally treated nanofiber webs at 1000 °C (Fig. 7.17e,f), 1500 °C, 2000 °C, and 2500 °C, there were no large changes in macromorphology, as in typical nongraphitizable carbon materials. When thermally treated up to 2800 °C (Fig. 7.17g,h), the main changes are a morphological transformation from a round to faceted cross-sectional morphology and from a smooth to wrinkled surface, mainly due to large density changes resulting from the liberation of heteroatoms and densification of carbon atoms (see the specific gravity change from 0.690 to 1.999 in Table 7.2). It is well known that the structural development of conventional carbon materials during thermal treatment is a thermally activated kinetic process [7.63]. When considering the morphological changes of our nano-sized fibers kinetically, compared with micro-sized ones, no large structural changes on isothermal treatment at 2500 °C and 2800 °C for various holding times ranging from 10 to 10–60 min are observed for our

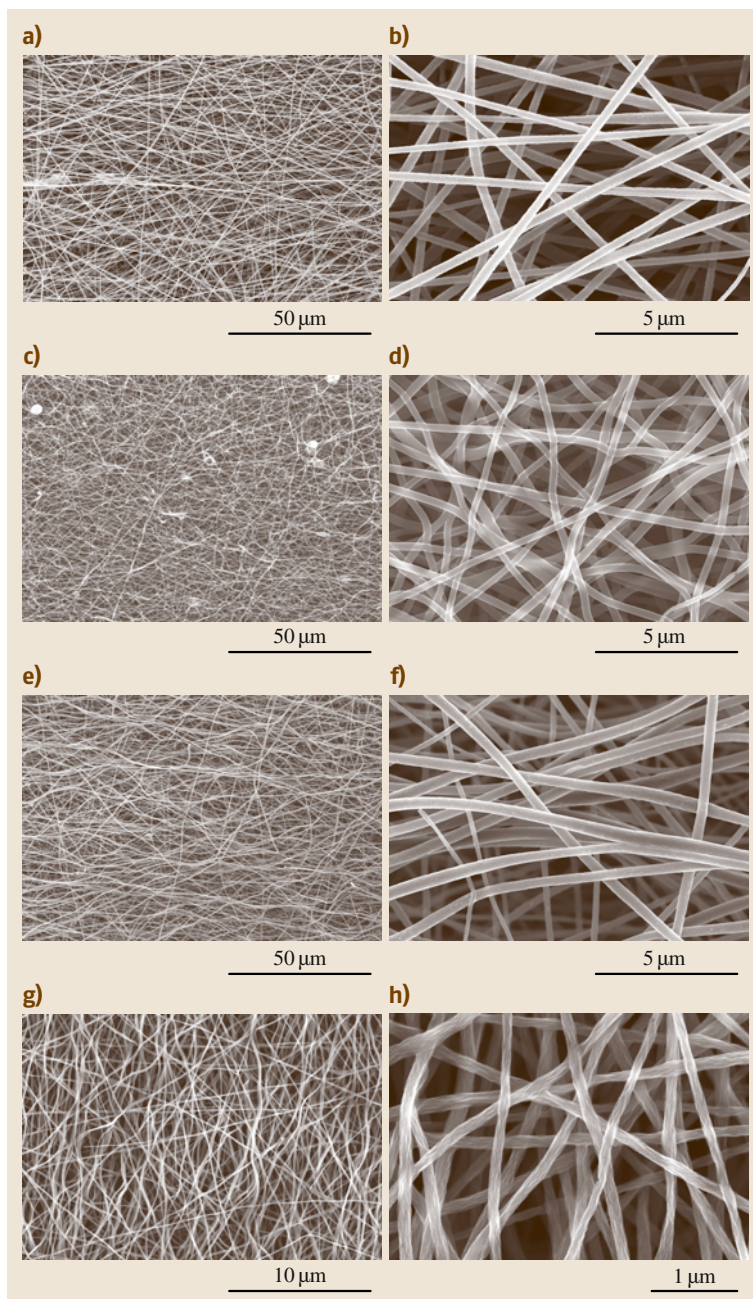


Fig. 7.17a–h FE-SEM images of (a,b) electrospun nanofibers thermally treated at (c,d) 700 °C, (e,f) 1000 °C, and (g,h) 2800 °C at different resolutions

electrospun nanofibers, because thermal energy is fully transferred to the inner part of the nanosized fibers within a short time. As a result, high-purity carbon nanofibers can be fabricated without disrupting the fiber morphology through the controlled combination

of electrospinning and thermal treatment, even when the electrospun nanofiber web is thermally treated up to 2800 °C.

The variations of structural changes on thermal treatment of electrospun nanofibers as a function

Table 7.2 Structural parameters and electrical conductivity for PAN-derived carbon nanofibers as a function of heat treatment temperature (HTT)

HTT (°C)	d_{002} (nm) ^a	L_c (nm) ^a	R value (I_D/I_G) ^b	Electrical conductivity (S/cm)	Specific gravity ^c
700	0.361	0.470	3.81	—	0.690
1000	0.362	0.498	3.41	2.193	—
1500	0.363	0.530	1.51	14.86	—
2000	0.359	0.777	1.31	55.41	—
2500	0.350	1.424	0.93	—	—
2800	0.341	5.274	0.29	20.15	1.998

^a Average interlayer spacing (d_{002}) and crystallite size (L_c) obtained by x-ray measurements using the Bragg and Scherrer formulae

^b R is the intensity of D band divided by the intensity of G band from Raman spectra

^c Specific gravity measured by Sartorius (Genius)

of heat treatment temperature have been studied by x-ray diffraction and microprobe Raman spectroscopy (Fig. 7.18a,b). The x-ray patterns near $2\theta = 25^\circ$ corresponding to the (002) layers of the graphite sharpen, and move to slightly higher angles for the sample at 2500 °C. In the Raman spectra (Fig. 7.18a), the increased intensity and decreased HWHM of the G band (E_{2g2} graphitic mode) at 1580 cm⁻¹, and also the decreased intensity and HWHM of the D band at 1355 cm⁻¹ (defect-induced mode), with increasing thermal treatment temperature indicate the sequential structural development [7.64]. Even when thermally treated at 2800 °C, the absence of (100) and (004) lines (Fig. 7.18b) and the presence of D band and the appearance of D' band (1620 cm⁻¹) (Fig. 7.18a) indicate that PAN-derived nanofibers are typically nongraphititi-

zable carbon. Structural parameters including electrical conductivity and specific gravity are summarized in Table 7.2. Even though no large changes are observed in the structural parameters (interlayer spacing and crystallite size) by x-ray diffraction for samples heat treated between 1000 °C and 1500 °C, it is noteworthy that large changes in the R value (from Raman spectra) occurred for the same samples. In addition, an abrupt increase in electrical conductivity, by more than one order of magnitude, occurs in this region. This inconsistency results from the different analytical techniques used, because XRD provides average bulk structural information whereas Raman studies provide structural information within the optical skin depth (≈ 10 nm). Thus, it is possible to say that carbonization occurs from the outer surface to the inner part kinet-

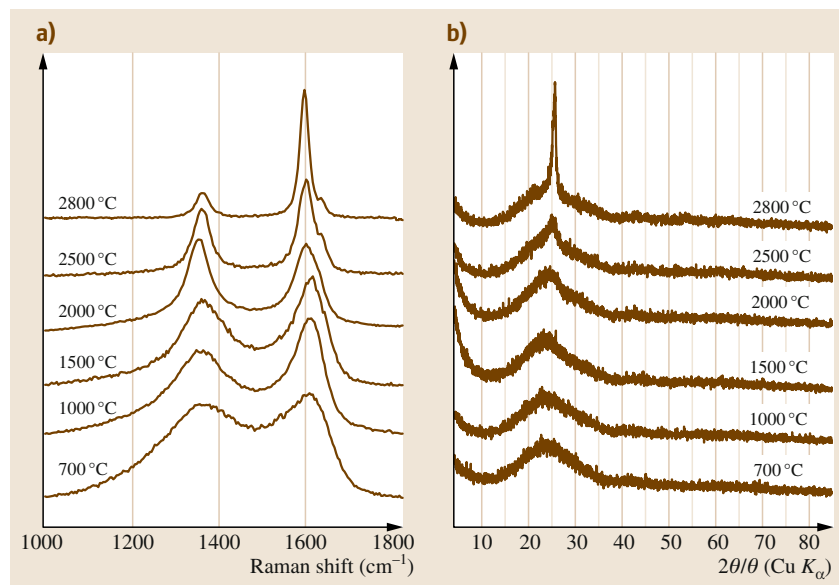


Fig. 7.18 (a) Raman spectra and (b) x-ray diffraction characterization of thermally treated nanofibers at various temperatures in the range 700–2800 °C

ically. Even though nanofiber web thermally treated at 2800 °C exhibits a relatively well-developed texture, the greatly decreased electrical conductivity (from 55.41 to 20.15 S/cm) is thought to be due to contact points between nanofibers due to abrupt volume changes. These structural parameters are not independent, but rather are interdependent. As a result, their very low graphitization ability, resulting from the intrinsic nature of the **PAN** polymer and their small diameter, is closely related to the electrochemical properties of the resulting electrochemical devices.

7.2.4 Electrospun Porous Carbon Nanofibers

Porous carbon materials have attracted much attention because of their versatile applications in catalysis, sensors, electronic devices, gas or liquid separation, and storage [7.65–70]. The conventional process for the production of porous carbon materials requires a pore creation step (so-called activation), which involves complex chemical and physical phenomena occurring on multiple time and temperature scales and is also expensive [7.71]. Against this background, intensive studies have been carried out to identify controllable and cost-effective synthetic routes such as the template method and use of polymer blends. The template technique has been utilized as a powerful tool to control pore sizes exactly in the nano to macro range [7.72–74]. The alternative for obtaining porous carbon materials is melt-spinning of immiscible polymer blends with subsequent thermal treatment [7.75–77]. In recent years, electrospinning has been shown to be a simple but powerful technique for preparation of functional nanofibers with submicrometer diameter [7.78]. There have been a few reports on preparation of electrospun carbon nanofibers from pure **PAN** [7.79–84], because **PAN** is a well-known precursor for conventional microsized carbon fibers [7.1–3]. Also, synthesis of fibrous carbons with a single and continuous hollow core has been reported by different groups using melt-spinning [7.85] and the co-electrospinning [7.86] of immiscible polymer blends with subsequent thermal treatments.

Thus, it is possible to fabricate porous but nanosized fibrous carbon materials in web form through nanofiber formation using the recently highlighted method of electrospinning of two immiscible polymer solutions and subsequent thermal treatment at 1000 °C in an inert atmosphere. Use of the electrospinning method enables production of nanosized (≈ 400 nm) organic fibers containing two separate

phases (sea and islands in cross-section) in web (or sheet) form, where the continuous phase (or sea) transforms into pore walls (or the skeleton of the nanofiber) and the discontinuous phase (or islands) forms multiple hollow pores that develop along the fiber length through thermal decomposition when thermally treated at 1000 °C.

Polymer blend solutions can be prepared by dissolving two or more different polymers in solvent, where phase separation into sea-island features occurs due to the intrinsic nature (e.g., interfacial tension, viscosity, elasticity) of the polymers [7.87]. Such stable emulsion-like polymer blend solutions are prepared by judicious selection of the two types of polymers, their blend ratios, and the solvent; the continuous phase (or sea) consists of **PAN** solution, and the homogeneously dispersed island-like phase consists of polymethylmethacrylate (**PMMA**) solution. Empirically, to understand the resulting morphological changes with the blend ratios and the nature of the constituent polymers, we have carried out viscosity and surface tension measurements for the polymer blends. All solutions showed shear-thinning behavior due to increasing orientation of drops along the flow direction at increasing shear rates. Also, the viscosity increased when the volume fraction of **PAN** in the blend solutions increased. Interestingly, we obtained lower surface tension for **PAN** solution (5.195 mN/m) than for **PMMA** solution (8.843 mN/m). Thus, the surface tension of our constituent polymers is thought to be the most important factor determining the cross-sectional morphology of the electrospun organic nanofibers. As a result, the low-surface-tension polymer (**PAN**) occupies the continuous phase (or sea) while the high-surface-tension polymer (**PMMA**) forms the discontinuous phase (or islands).

Thus, we were able to obtain homogeneous and long organic nanofibers in the form of a thin white web through use of optimized electrospinning conditions. The conversion of an organic nanofiber into a carbon nanofiber involves stabilization and thermal treatment steps. Air stabilization of electrospun nanofibers, which involves complex chemical reactions such as three-dimensional cross-linking, is accompanied by a change in color from white to reddish brown. Finally, by thermally treating the air-stabilized fibers, we obtain a black web consisting of fibrous carbon containing multiple hollow cores.

As shown in Fig. 7.19a–c, the electrospun organic nanofibers exhibit a smooth outer surface, a long fibrous morphology, and a homogeneous diameter distribution in the range 200–400 nm. The higher the fraction of

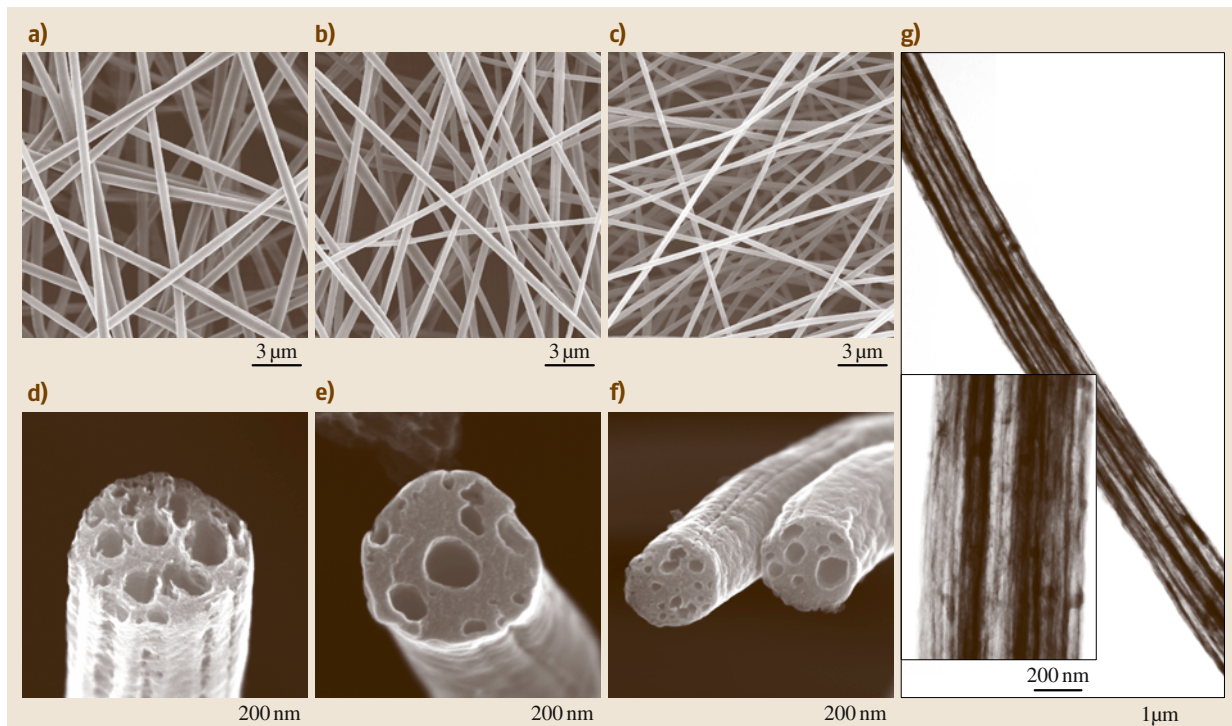


Fig. 7.19 (a–c) Macromorphologies of electrospun polymeric nanofibers containing two polymer phases (PAN/PMMA = (a) 5/5, (b) 7/3, and (c) 9/1), and cross-sectional FE-SEM images of nanofibers thermally treated at 1000 °C (PAN/PMMA = (d) 5/5, (e) 7/3, and (f) 9/1). (g) TEM image of the sample shown in (d) (PAN/PMMA = 5/5), showing linearly developed multiple hollow cores along the fiber length (*inset* shows a magnified TEM image)

PAN polymer, the smaller the diameter of the obtained nanofibers, basically due to their high ability to form fibers (or spinnability). Here it is noted that an electrospun organic single nanofiber consists of two phases, namely the discontinuous and long rod-like PMMA phase and the continuous PAN phase. Then, we carried out studies of the air stabilization of electrospun nanofiber web at 280 °C for 1 h under controlled air circulation, which is critical to sustain their fibrous morphology through the introduction of dimensional stability. Therefore, the fibrous morphology is not disrupted by the following thermal treatment step at 1000 °C in an inert atmosphere, as in the case of conventional PAN-based carbon fiber. Since the elongated PMMA phase decomposes (or disappears) without carbon residue and the continuous PAN phase was easily transformed into carbon ($\approx 40\text{--}50\%$) during thermal treatment, we successfully created multiple hollow cores within a single carbon fiber. As shown by the cross-sectional SEM images of carbon

fibers thermally treated at 1000 °C in Fig. 7.19d–f, multiple hollow cores were present in a single carbon fiber. Interestingly, the number of hollow cores increased with increasing PMMA concentration. In addition, low-resolution TEM images (Fig. 7.19g) indicated that the long but discontinuous multiple hollow cores are well developed along the fiber length. Thus, we are able to control the diameter, number, and length of hollow cores in a single carbon nanofiber using well-known polymer chemistry knowledge. Finally, the rugged surface morphology of the thermally treated carbon nanofibers (Fig. 7.19d–f) is believed to be the combined result of abrupt gas evolution of both polymers and also the carbon densification process. Therefore, it is expected that the blend ratio of the constituent polymers will greatly affect the patterns of pore creation as well as the porosity of the carbon nanofibers.

On detailed TEM study after thermal treatment at 2800 °C, the outer surface of all samples was

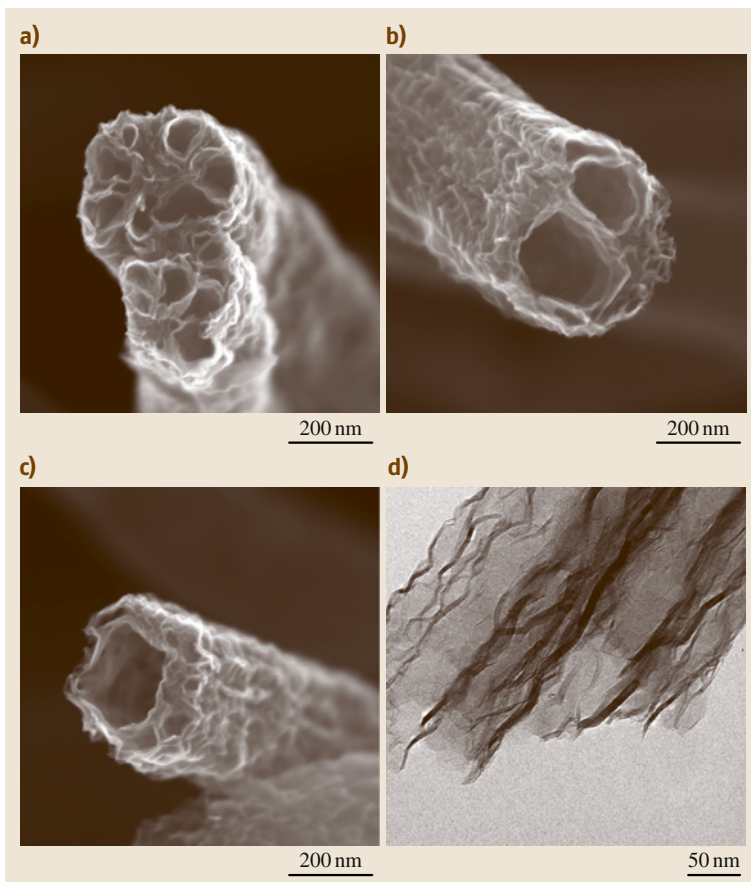


Fig. 7.20a–d Cross-sectional images of nanofibers thermally treated at 2800 °C (PAN/PMMA = (a) 5/5, (b) 7/3, and (c) 9/1); (d) TEM image of the sample shown in (a), showing multicore wall structurally developed through thermal treatment

transformed from relatively rugged to largely irregular because of the large changes in real density resulting from the high-temperature treatment. It is interesting to note that the multiple hollow cores in

a single fiber did not collapse (Fig. 7.20a–c) and that the pore walls/skeletons (≈ 10 nm), consisting of ca. 15 graphene sheets, were crystalline on the short range but undulated along the fiber length (Fig. 7.20d).

7.3 Applications of Carbon Nanofibers

The particular characteristics of carbon nanofibers due to their small dimension, excellent physicochemical properties, and relatively low cost make them useful in versatile applications ranging from multifunctional composites, electrode materials for supercapacitors, anode electrodes or additives for lithium-ion batteries, supporting materials for metal particles, to bone tissue scaffolds. In this section, we present some of the important applications of carbon nanofibers.

7.3.1 Electrode Material in Lithium-Ion Secondary Batteries

Since sp^2 -based carbon materials were adopted as anode materials in commercialized lithium-ion batteries (LIBs) to solve safety problems, various types of carbon textures have been examined to improve the specific energy and power density of batteries [7.88–92]. The capacity as well as cyclic performance of LIBs strongly depend on the carbon texture due to the very different

lithium-ion (Li^+) insertion and desorption mechanisms. More recently, development of high-power LIBs has been required to meet growing demand for use in lighter electronic portable devices and hybrid electric vehicles (HEV). Thus, intensive study has been focused on nanosized carbon materials as promising materials for storing Li^+ , because they show increased capacity as an active material and also improved cyclic characteristics when used as an additive to anode and cathode materials [7.93–100].

Through the right combination of the electrospinning technique and thermal treatment process, dimensionally thin, mechanically tough, electrically conductive web-based electrodes consisting of interconnected nanofibers with a diameter in the range 200–300 nm have been fabricated. No binder or conductive filler (e.g., polyvinylidene fluoride, carbon black) was used in the fabrication of the active electrode, to enable evaluation of the anodic performance of the electrospun carbon nanofiber web. Therefore, the thin web in combination with their expected good mechanical and electrical properties makes them very attractive for fabrication of anode materials in thin polymer LIBs. Figure 7.21 shows voltage profiles for nanofiber webs thermally treated at 700 °C, 1000 °C, and 2800 °C. Even though carbon nanofibers thermally treated at 700 °C and 1000 °C have large Li^+ storage capacity of 510 and 1000 mAh/g, their reversible capacities are 300 and 450 mAh/g, respectively. Their large irreversible capacities (≈ 500 mAh/g) are closely related to electrolyte decomposition and the formation

of a solid electrolyte interphase at ≈ 0.8 V [7.101]. However, after the second cycle, relatively stable reversible capacity could be obtained. Nanofiber web thermally treated at 2800 °C exhibits a reproducible discharge/charge plateau at about 0.2 V (stage formation) and provides a reversible capacity of 130 mAh/g. As mentioned above, thermally treated PAN polymer could be characterized as a typical nongraphitic carbon, and thus has low discharge capacity due to its low crystallinity. It is noteworthy that carbon nanofibers thermally treated at 1000 °C have reversible capacity of 450 mAh/g, which is larger than both the theoretical value for graphite (372 mAh/g) and the value of 300 mAh/g for carbon nanofiber thermally treated at 700 °C.

Very recently, Yoon et al. [7.102] reported high capacity of 431 mAh/g for highly crystalline carbon nanofibers through the catalytic chemical vapor deposition method by carrying out a systematic study of the anodic behaviors of very different crystalline and textured carbon nanofibers. Also, relatively crystalline carbon nanofibers obtained by applying direct-current (DC) high voltage to a mist of 2-propanol showed a large reversible capacity of ≈ 340 mAh/g [7.103]. It is not clear why the reversible capacity of our carbon nanofiber thermally treated at 1000 °C exhibited the largest reversible capacity of 450 mAh/g as compared with various carbon nanofibers including microsized PAN carbon fiber (≈ 220 mAh/g) [7.104]. One possible explanation is that the nanosized fiber morphology invokes different carbonization behavior including gas

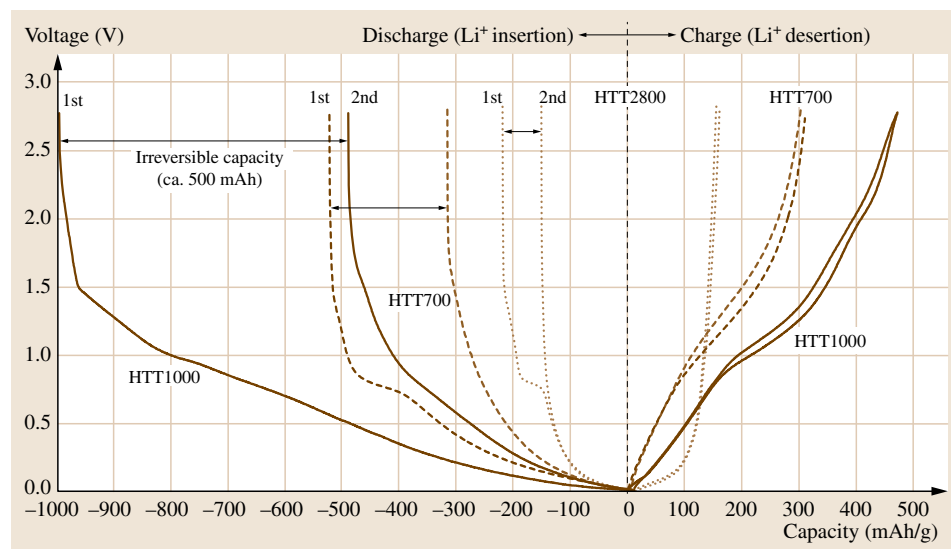


Fig. 7.21 Charge-discharge curves for nanofiber webs thermally treated at 700 °C, 1000 °C, and 2800 °C (current density 30 mA/g, second cycle)

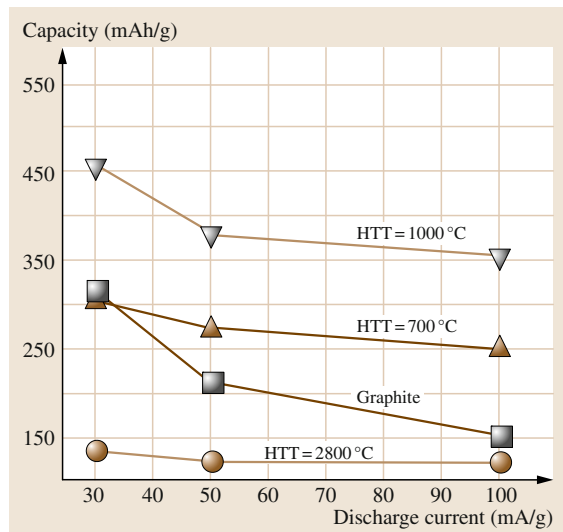


Fig. 7.22 Variation of reversible capacities (rate capability) for nanofiber webs thermally treated at 700 °C, 1000 °C, and 2800 °C at different discharge current densities of 30, 50, and 100 mA/g ▶

pacitances strongly depend on the types and forms of the electrode materials. Against this background, various forms and textures of porous carbon have been examined as possible electrode materials for supercapacitors [7.106–111]. Among these, carbon nanotubes have attracted lots of attention, because they have large accessible surface area, based on their nanosized diameter, and relatively high electrical conductivity, which makes them very promising as efficient electrode materials for use in high-power supercapacitors [7.112–116]. Currently, their intrinsic problems, such as the limited amount of available charge and high cost, combined with their low effective specific surface area, limit practical use of carbon nanotubes as the electrode material in supercapacitors.

Another route to the fabrication of fibrous carbon as the electrode material for supercapacitors, based on electrospinning and subsequent steam activation, has been reported [7.33]. The preparation process involves fiber formation from a PAN polymer solution using electrostatic force. The technical reason for selecting PAN as a precursor was the good electrosprinnability of PAN polymer solution and the relatively high carbon yield. The subsequent physical activation to increase the specific surface area or to create pores by subjecting air-stabilized carbon to steam at high temperature involves complex chemical and physical phenomena occurring on multiple time and temperature scales, and this step was known to be difficult in terms of controlling the pore size and surface properties of the obtained carbon materials, as well as being time consuming [7.117–119].

When considering their versatile promising applications in catalysis, electrochemical energy storage systems, and gas or liquid separation and storage, a simple and effective technique for decreasing the fiber diameter of ≈ 100 nm and also creating effective pores in a controllable fashion has to be developed to maximize the intrinsic 1-D functions (e.g., large accessible surface area and enhanced electrical and mechanical properties). Here we report a method for preparing porous, smaller-sized fibrous carbon in thin web form with the help of zinc chloride. Specifically, zinc chloride decreases the fiber diameter from 350 to 200 nm during electrospinning, enhances the reaction rate catalytically during air stabilization, and effectively creates suitable pores on the outer surface of smaller-sized (≈ 100 nm) carbon

evolution and pore development and thereby different surface properties when compared with microsized polymeric materials. In other words, the higher reversible capacity (up to 450 mAh/g) is expected to originate from the peculiar microtexture of carbon nanofibers thermally treated at 1000 °C, e.g., the highly disordered structure, defects, and dangling bonds. Thus, Li ions are inserted/deserted into and out of carbon nanofibers by a doping/dedoping process, because we could not observe any distinct redox peaks from the derivative voltage profiles (not shown here). This takes into account that a nanofiber web treated at low temperature (700 °C and 1000 °C) with constant and slightly inclined charge potential profiles is quite suitable for electronic portable device and HEV applications due to easy distinction of the remaining battery capacity. In addition, when considering the battery rate capability (30, 50, and 100 mA/g) of samples thermally treated at 700 °C, 1000 °C, and 2800 °C (Fig. 7.22), there was no large degradation of capacity as a function of discharge current density compared with conventional graphite. In other words, this result confirms that the Li^+ diffusion path within anode materials is greatly reduced due to the small diameter of the carbon nanofibers.

7.3.2 Electrode Material for Supercapacitors

Supercapacitors have been intensively investigated as a main and/or backup energy storage systems, because they are able to carry high power and, furthermore, to have a long lifecycle [7.105]. Their double-layer ca-

nanofibers during thermal treatment. Also, dimensionally thin but flexible, an electrically conductive black web consisting of physically entangled, long carbon nanofibers enabled us to fabricate highly pure and self-sustained electrodes, without using binder or conductive materials; furthermore, the suitably developed micropores as well as the large external surface directly contributed to good capacitive behavior of supercapacitors.

The resultant black web, consisting of porous and long carbon nanofibers with diameter of 100 nm, was cut into a rectangular (2.25×2.25 cm) shape, and then attached to nickel plates to evaluate the capacitive performance based on a two-electrode system. The electrochemical properties of the carbon nanofiber web electrodes were studied by cyclic voltammetry in 6 M KOH aqueous solution as an electrolyte. Typical cyclic voltammograms (CVs) at 10–200 mV/s scan rate are shown in Fig. 7.23. The CVs were recorded in the potential range between 0 and 0.9 V, where no obvious redox peaks originating from the functional groups are observed. It is well known that CVs for an ideal double-layer capacitor are characterized by a perfectly rectangular-shaped profile [7.105]. For our samples, the CV profiles deviated from this ideal shape, but the shape of the curve is still satisfactory, even at the high scan rate used. However, the relatively broad feature in the CV of all samples could be considered as a side-reaction closely related to the intrinsic nitrogen functionalities derived from the parent PAN and also oxygen functional groups formed by zinc chloride.

When the zinc chloride was increased from 1% to 5%, the specific capacitances, calculated from CV

curves, increase from 120 to 140 F/g without any distinct changes in the shape of the CV profiles (Fig. 7.24a), indicating not only a reduction in the equivalent series resistance of the nanofiber web electrode, but also a reduction in the hindrance of ion penetration into the pores. The specific capacitance of our sample was higher than that of freestanding multi-walled carbon nanotubes in KOH medium (≈ 113 F/g) [7.112]. In addition, the samples showed relatively high rate capability (Fig. 7.24a). In other words, the sample exhibited good capacitive behavior with low diffusive limitation compared with conventional activated carbon materials, which could be explained by the highly intermingled porous nanofiber network providing an easily available electrode–electrolyte interface to form an electric double layer.

We measured the alternating-current (AC) impedance spectra (Nyquist plot) (Fig. 7.24b), because this technique enables one to distinguish the resistance and capacitance of devices. The impedances nearest to the origin were determined at high frequencies. This plot consists of three main regions (inset to Fig. 7.24b):

- (I) A semicircular arc representing the resistance and capacitance of the contact between the electrode and current collector, and the resistance of the porous electrode itself.
- (II) Another, small semicircular arc corresponding to the movement of electrons across the electrical double layer.
- (III) A (near-vertical) straight line at low frequency, suggesting blocking electrode behavior. This very

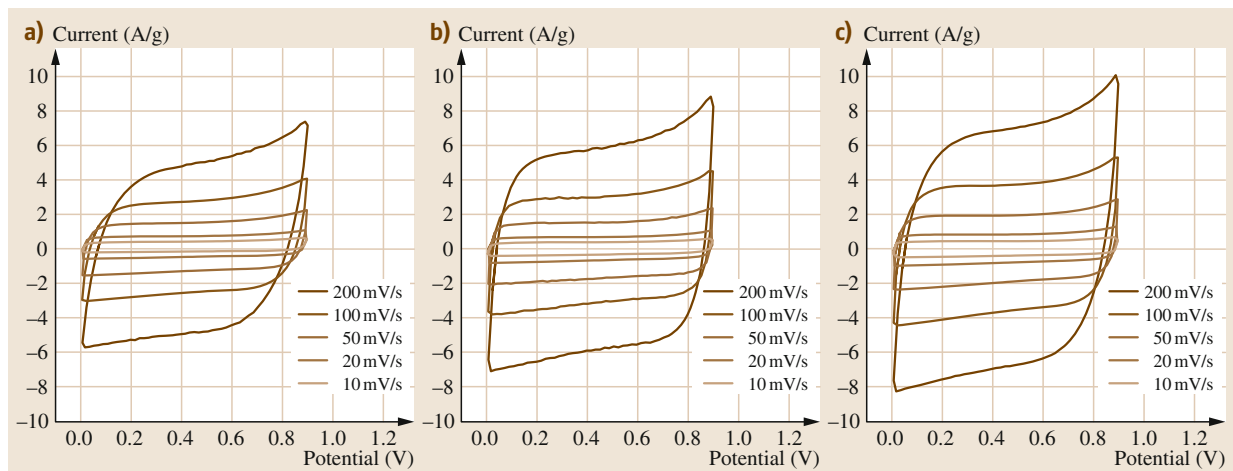


Fig. 7.23a–c Cyclic voltammograms of zinc-chloride-activated porous carbon nanofibers; (a) 1 wt %, (b) 3 wt %, and (c) 5 wt % zinc-chloride-activated porous nanofiber webs in 6 M KOH solution at different sweep rates

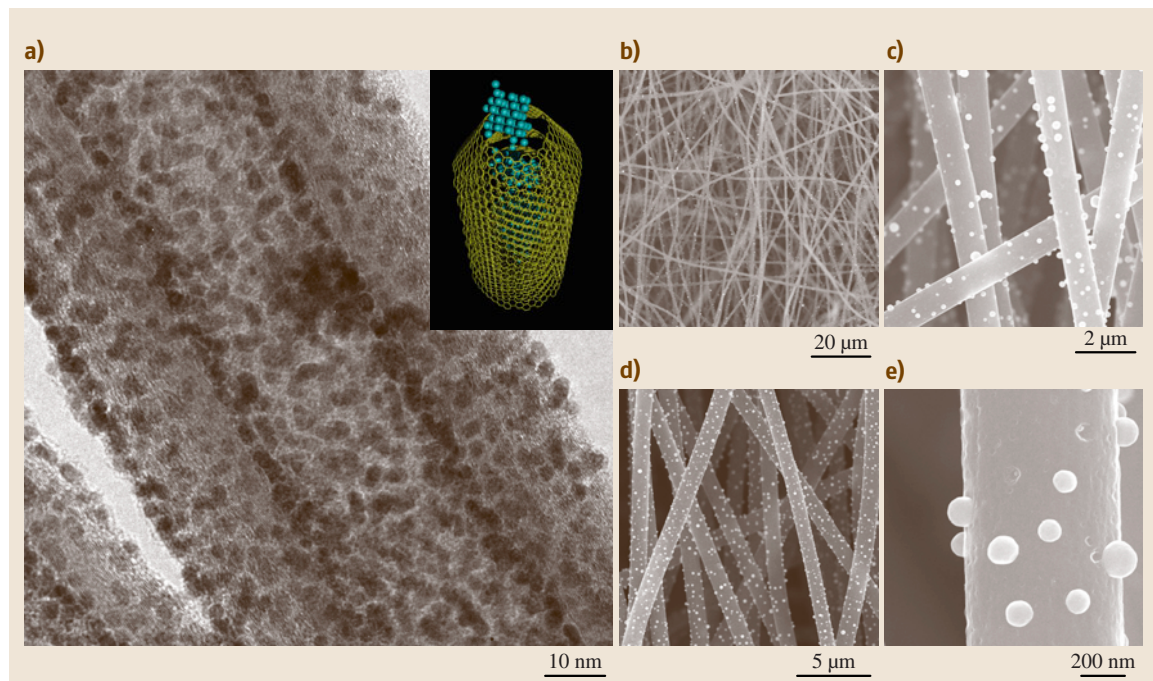
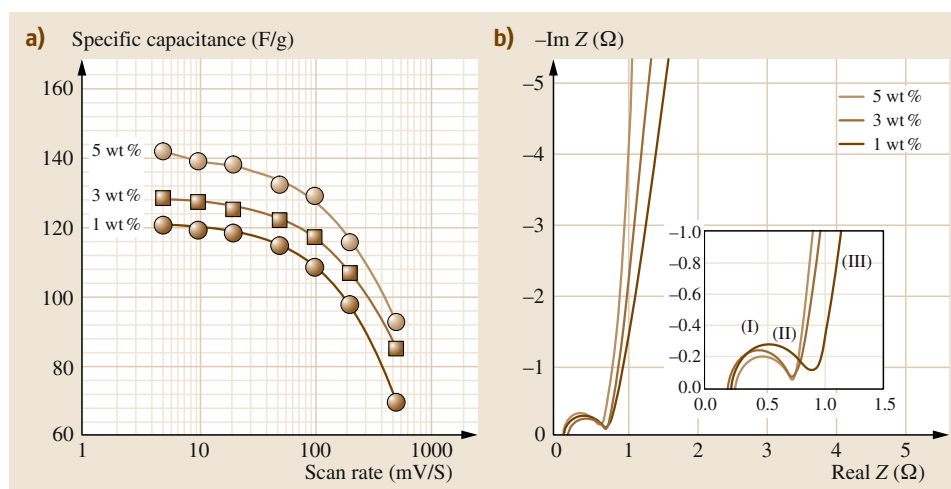


Fig. 7.25 (a) HRTEM image exhibiting high dispersion of Pt nanoparticles only on the surface of a carbon nanofiber. **(b–e)** SEM images of electrospun-based carbon nanofibers at different resolutions. Note that spherical palladium particles homogeneously cover the outer surface of the carbon nanofibers

steep spike shows that the kinetics of the diffusion of ions in the solution as well as the adsorption of ions onto the electrode surface occur swiftly. Therefore, the Warburg impedance, representing the diffusion of ions in pores and in the electrolyte, is unnoticeable.

The values I and II (inset of Fig. 7.24b) gradually decrease with increasing zinc chloride content from 1 wt % to 5 wt %, respectively. Electrolyte accessibility becomes greater for the larger pores, while the ions will not enter the smallest pores. Thus, lower resistance is associated with better electrolyte pore accessibility. In

the case of the sample with 5 wt % added zinc chloride, the pore density is higher than for the others, which is why the capacitive behavior appears at lower resistance.

7.3.3 Supporting Material for Metal Nanoparticles

For a decade, nanocarbon materials have been widely studied as catalyst supports for use in heterogeneous

catalysis due to their unique morphology and reactivity [7.120–122]. It is well known that the basic properties of impregnated catalyst are strongly affected by the impregnation method, microstructure, surface reactivity, and the metal precursor [7.123, 124]. Among these factors, appropriate morphology and nanostructure of the support is considered to be the main factor enabling the production of a well-dispersed nanoparticle catalyst as in Fig. 7.25.

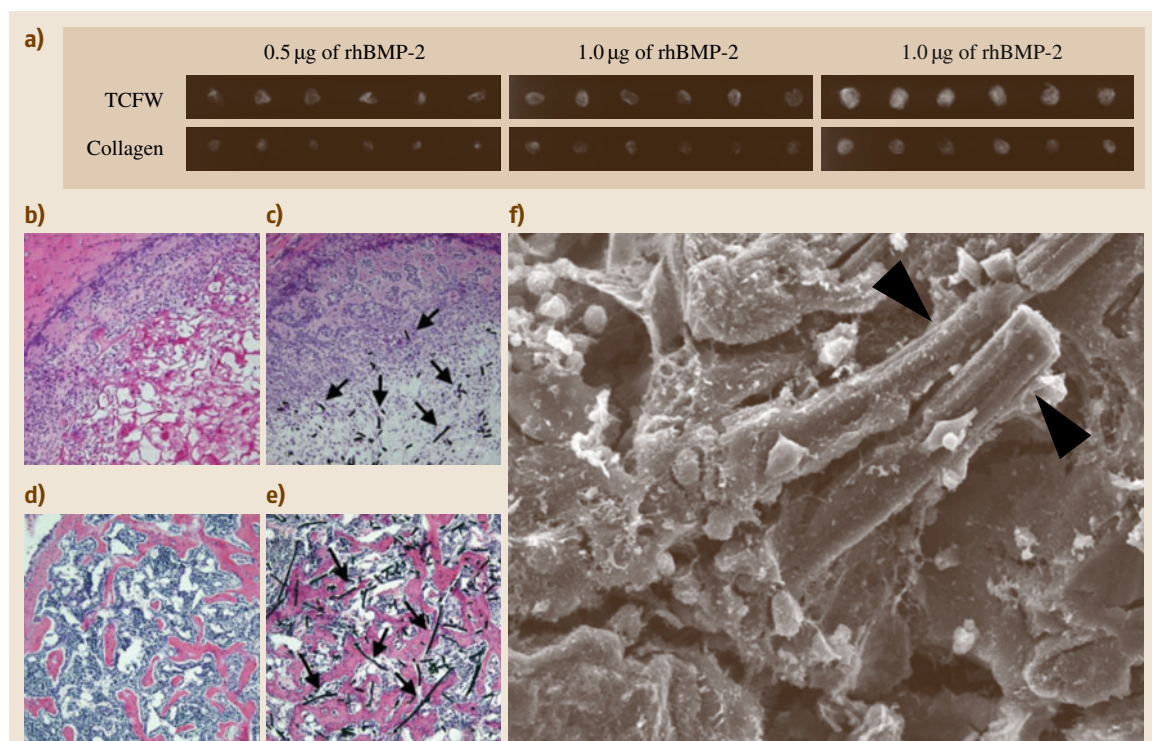


Fig. 7.26a–f Ectopic bone formation in the dorsal muscle of mice. (a) X-ray images of ectopic bone formed by rhBMP-2/carbon nanofiber web and rhBMP-2/collagen implants. Three weeks later, bone trabecular shadows were observed in all of the carbon nanofiber web and collagen implants with 0.5, 1 or 5 mg rhBMP-2. The bone trabecular shadows were clear and large and corresponded to the rhBMP-2 dosage in both groups. At each dose, the shadows of the carbon nanofiber web group were larger than those of the collagen group. (b–e) Bone formation of the carbon nanofiber web and collagen implants with 5 mg rhBMP-2. At 1 week, both the rhBMP-2/collagen (b) and rhBMP-2/carbon nanofiber web (c) showed the presence of immature bone matrix in the peripheral zone of the implants. The maturity of the collagen and carbon nanofiber web groups was the same. At 3 weeks, both the rhBMP-2/collagen (d) and rhBMP-2/carbon nanofiber web (e) specimens demonstrated normal-appearing bone with thick trabecular and hematopoietic marrow. Mature trabecular of the carbon nanofiber web group was thicker than in the collagen group. The collagen sheets were absorbed, but the carbon nanofibers remained and were in dense contact with the bone matrix. Hematoxylin and eosin staining. Scale bar: 200 µm. Arrows: carbon fibers. (f) SEM image of tissue sections containing the carbon nanofiber web with 5 mg rhBMP-2 at 3 weeks after operation. The carbon fibers were directly integrated into the new bone and adhered closely to the bone matrix with no intervening space. Scale bar: 10 µm. Arrow heads: carbon nanofibers

Efficient impregnation of Pt nanoparticles (outer diameter < 3 nm) into carbon nanofibers has been reported [7.125]. The method involves dispersion of the nanofibers in H₂PtCl₆, followed by low-temperature annealing. The Pt particle deposition is homogeneous, and can be controlled selectively on the outer or internal core using the hydrophobic nature of the material (Fig. 7.25a). Since the activity of the Pt nanoparticles on the fibers is high, this material could find application in efficient catalysts and allied biological devices. Alternatively, carbon nanofibers containing palladium nanoparticles have been prepared simply by electrospinning polymer solution containing palladium chloride and subsequent thermal treatment in argon [7.126]. It has been demonstrated that palladium oxide formed during air stabilization transforms into nanoparticles through an interaction with the carbon material. Since the palladium nanoparticles homogeneously covering the outer surface of the nanofibers (Fig. 7.25b–e) are small enough to have high catalytic activity, this material could find application in efficient catalysts and hydrogen sensors.

7.3.4 Bone Tissue Scaffold

At present, the most popular scaffold is type I collagen [7.127–129], which is often used in clinical applications [7.130, 131]. However, use of collagen leads to certain problems such as the possibility of disease transfer or immunogenic reactions due to xenogenicity [7.132–134]. Further, the soft nature of collagen does not allow it to preserve its shape in the

body. Actually, carbon fibers have been used for tendon repair in clinical settings [7.135, 136], but they are too thick for use in cell or cytokine therapy for tissue regeneration. If creation of a three-dimensional web consisting of carbon fibers with a nanostructure is possible, it may serve as a promising new scaffold biomaterial for tissue regeneration. Thus, by using the electrospinning method, a carbon nanofiber web consisting of high-purity carbon was examined as a bone tissue scaffold [7.35]. The carbon nanofiber web consists of high-purity carbon with a very small amount of functional groups. It is considered to be safe in the living body even when present at high levels. In vivo implantation for a short time period resulted in little inflammatory reaction of the surrounding tissue, indicating that this material is highly biocompatible. Examination of the interface between the carbon fibers and bone matrix by using FE-SEM revealed that the carbon fibers directly adhered to the bone itself without any intervening space being integrated into the bone matrix, indicating high bone tissue compatibility. Recombinant human bone morphogenic protein-2 (rhBMP-2)/nanofiber web composite implants could induce ectopic new bone formation effectively when tested in vivo and could repair large bone defects orthotopically (Fig. 7.26). It is envisaged that the nanofiber web is a promising scaffold material candidate for use in bone regeneration therapy and represents a prominent advance in technology for enhancement of bone repair. We also expect that such carbon-nanofiber-derived scaffold systems will play a major role in regeneration therapy for various tissues in future clinical applications.

7.4 Conclusions

The 19th century can be remembered as the iron age, while the 20th century is recognized as being founded on silicon technology. Now, much attention is being paid to fibrous nanocarbon materials as one of the promising candidates that could revolutionize technology in the 21st century. Carbon nanofibers differ from conventional carbon fibers in their nanosized diameter and from carbon nanotubes in their intrinsic geometry. Thus, they could be visualized as connecting bridges between molecular and macro materials. However, some

challenges have to be solved in order to speed up industrial use of carbon nanofibers. The first challenge is large-scale synthesis of defect-free carbon nanofibers at low cost. Secondly, it is important to control the diameter and length of carbon nanofibers. The final and most important challenge is how to manipulate (or disperse) such nanosized entangled fluffy materials in order to fabricate novel multifunctional materials. It is envisaged that various carbon-nanofiber-based products will be seen in less than 10 years.

References

- 7.1 J.B. Donnet, R.C. Bansal: *Carbon Fibers* (Marcel Dekker, New York 1984)
- 7.2 L.H. Peebles: *Carbon Fibers* (CRC, Boca Raton 1994)
- 7.3 D.D.L. Chung: *Carbon Fiber Composites* (Butterworth Heinemann, Boston 1994)
- 7.4 M.S. Dresselhaus, G. Dresselhaus, K. Sugihara, I.L. Spain, H.A. Goldberg: *Graphite Fiber and Filaments* (Springer, Berlin Heidelberg 1988)
- 7.5 A. Oberlin, M. Endo, T. Koyama: Filamentous growth of carbon through benzene decomposition, *J. Cryst. Growth* **32**, 335–349 (1976)
- 7.6 R.T.K. Baker: Catalytic growth of carbon filaments, *Carbon* **27**, 315–323 (1989)
- 7.7 G.G. Tibbetts: Why are carbon filaments tubular?, *J. Cryst. Growth* **66**, 632–637 (1984)
- 7.8 M. Endo: Grow carbon fibers in the vapor phase, *Chem. Technol.* **18**, 568–576 (1988)
- 7.9 N.M. Rodriguez: A review of catalytically grown carbon nanofibers, *J. Mater. Res.* **8**, 3233–3250 (1993)
- 7.10 G.G. Tibbetts: Vapor-grown carbon fibers: Status and prospects, *Carbon* **27**, 745–747 (1989)
- 7.11 S. Iijima: Helical microtubules of graphitic carbon, *Nature* **354**, 56–58 (1991)
- 7.12 M.S. Dresselhaus, G. Dresselhaus, P. Eklund: *Science of Fullerenes and Carbon Nanotubes* (Academic, New York 1996)
- 7.13 R. Saito, G. Dresselhaus, D.S. Dresselhaus: *Physical Properties of Carbon Nanotubes* (Imperial College Press, London 1998)
- 7.14 T.W. Ebbesen: *Carbon Nanotubes: Preparation and Properties* (CRC, London 1997)
- 7.15 N.M. Rodriguez, A. Chambers, R.T.K. Baker: Catalytic engineering of carbon nanostructures, *Langmuir* **11**, 3862–3866 (1995)
- 7.16 M. Endo, Y.A. Kim, T. Fukai, T. Hayashi, K. Oshida, M. Terrones, T. Yanagisawa, S. Higaki, M.S. Dresselhaus: Structural characterization of cup-stacked type nanofibers with an entire hollow core, *Appl. Phys. Lett.* **80**, 1267–1269 (2002)
- 7.17 S.H. Yoon, S. Lim, Y. Song, Y. Ota, W.M. Qiao, A. Tanaka, I. Mochida: KOH activation of carbon nanofibers, *Carbon* **42**, 1723–1729 (2004)
- 7.18 S.H. Yoon, C.W. Park, H.J. Yang, Y. Korai, I. Mochida, R.T.K. Baker, N.M. Rodriguez: Novel carbon nanofibers of high graphitization as anodic materials for lithium ion secondary batteries, *Carbon* **42**, 21–32 (2004)
- 7.19 Q.F. Liu, W.C. Ren, Z.G. Cheng: Semiconducting properties of cup-stacked carbon nanotubes, *Carbon* **47**, 731–736 (2009)
- 7.20 M. Endo, Y.A. Kim, M. Ezaka, K. Osada, T. Yanagisawa, T. Hayashi, M. Terrones, M.S. Dresselhaus: Selective and efficient impregnation of metal nanoparticles on cup-stacked-type nanofibers, *Nano Lett.* **3**, 723–726 (2003)
- 7.21 Y.K. Choi, Y. Gotoh, K.I. Sugimoto, S.M. Song, T. Yanagisawa, M. Endo: Processing and characterization of epoxy nanocomposites reinforced by cup-stacked carbon nanotubes, *Polymer* **46**, 11489–11498 (2005)
- 7.22 T. Yokozeki, Y. Iwahori, S. Ishiwata: Matrix cracking behaviors in carbon fiber/epoxy laminates filled with cup-stacked carbon nanotubes (CSCNTs), *Compos. A: Appl. Sci. Manuf.* **38**, 917–924 (2007)
- 7.23 T. Yokozeki, Y. Iwahori, S. Ishiwata, K. Enomoto: Mechanical properties of CFRP laminates manufactured from unidirectional preprints using CSCNT-dispersed epoxy, *Compos. A: Appl. Sci. Manuf.* **38**, 2121–2130 (2007)
- 7.24 T. Yokozeki, Y. Iwahori, M. Ishibashi, T. Yanagisawa, K. Imai, M. Arai, T. Takayashi, K. Enomoto: Fracture toughness improvement of CFRP laminates by dispersion of cup-stacked carbon nanotubes, *Compos. Sci. Technol.* **69**, 2268–2273 (2009)
- 7.25 K. Saito, M. Ohtani, F. Fukuzumi: Electron-transfer reduction of cup-stacked carbon nanotubes affording cup-shaped carbons with controlled diameter and size, *J. Am. Chem. Soc.* **128**, 14216–14217 (2006)
- 7.26 T. Hasobe, H. Murata, P.V. Kamat: Photoelectrochemistry of stacked-cup carbon nanotube film: Tube-length dependence and charge transfer with excited porphyrin, *J. Phys. Chem. C* **111**, 16626–16634 (2007)
- 7.27 S. Ramakrishna, K. Fujihara, W.-E. Teo, T.-C. Lim, Z. Ma: *An Introduction to Electrospinning and Nanofibers* (World Scientific, Singapore 2005)
- 7.28 D.H. Reneker, A.L. Yarine, H. Fong, S. Koombhongse: Bending instability of electrically charged liquid jets of polymer solutions in electrospinning, *J. Appl. Phys.* **87**, 4531 (2000)
- 7.29 Y.M. Shin, M.M. Hohman, G.C. Martin: Processing and microstructural characterization of porous biocompatible protein polymer thin films, *Polymer* **40**, 7397–7407 (1999)
- 7.30 I.D. Norris, M.M. Shaker, F.K. Ko, A.G. MacDiarmid: Electrostatic fabrication of ultrafine conducting fibers: polyaniline/polyethylene oxide blends, *Synth. Met.* **114**, 109–114 (2000)
- 7.31 F. Ko, Y. Gogotsi, A. Ali, N. Naguib, H. Ye, G. Yang, C. Li, P. Willis: Electrospinning of continuous carbon nanotube-filled nanofiber yarns, *Adv. Mater.* **15**, 1161–1165 (2003)
- 7.32 C. Vozzi, C.J. Flaim, F. Bianchi, A. Ahluwalia, S. Bhatia: Microfabricated PLGA scaffolds: a comparative study for application to tissue engineering, *Mater. Sci. Eng.* **20**, 43–47 (2002)
- 7.33 C. Kim, K.S. Yang: Electrochemical properties of carbon nanofiber web as an electrode for supercapacitor prepared by electrospinning, *Appl. Phys. Lett.* **83**, 1216–1218 (2003)

- 7.34 R. Dersch, M. Steinhart, U. Boudriot, A. Greiner, J.H. Wendorff: Nanoprocessing of polymers: applications in medicine, sensors, catalysis, photonics, *Polym. Adv. Technol.* **16**, 276–282 (2005)
- 7.35 K. Aoki, Y. Usui, N. Narita, N. Ogiwara, N. Iashigaki, K. Nakamura, H. Kato, K. Sano, N. Ogiwara, K. Kametani, C. Kim, S. Taruta, Y.A. Kim, M. Endo, N. Saito: A thin carbon fiber web as a scaffold for bone tissue regeneration, *Small* **5**, 1540–1546 (2009)
- 7.36 C. Kim, K.S. Yang, M. Kojima, K. Yoshida, Y.J. Kim, Y.A. Kim, M. Endo: Fabrication of electrospun-derived carbon nanofiber web for the anode material of lithium-ion secondary batteries, *Adv. Funct. Mater.* **16**, 2393–2397 (2006)
- 7.37 R. Bacon: Production of graphite whiskers, *J. Appl. Phys.* **31**, 283–290 (1960)
- 7.38 M. Endo, R. Saito, M.S. Dresselhaus, G. Dresselhaus: From carbon fibers to carbon nanotubes. In: *Carbon Nanotubes*, ed. by T.W. Ebbesen (CRC, New York 1997) pp. 35–105
- 7.39 A. Oberlin: High-resolution TEM studies of carbonization and graphitization, *Chem. Phys. Carbon* **22**, 1–135 (1989)
- 7.40 L.H. Peebles, Y.G. Yanovsky, A.G. Sirota, V.V. Bogdanov, P.M. Levit: Mechanical properties of carbon fibers. In: *Carbon Fibers*, ed. by J.B. Donnet (Marcel Dekker, New York 1998) pp. 311–370
- 7.41 M. Endo, Y.A. Kim, T. Hayashi, K. Nishimura, T. Matsuhashita, K. Miyashita, M.S. Dresselhaus: Vapor-grown carbon fibers (VGCFs): basic properties and battery application, *Carbon* **39**, 1287–1297 (2001)
- 7.42 M. Endo, K. Takeuchi, K. Kobori, K. Takahashi, H.W. Kroto, A. Sarkar: Pyrolytic carbon nanotubes from vapor-grown carbon fibers, *Carbon* **33**, 873–881 (1995)
- 7.43 H.J. Dai, A.G. Rinzler, P. Nikolaev, A. Thess, D.T. Colbert, R.E. Smalley: Single-wall nanotubes produced by metal-catalyzed disproportionation of carbon monoxide, *Chem. Phys. Lett.* **260**, 471–475 (1996)
- 7.44 C.N.R. Rao, R. Sen, B.C. Satishkumar, A. Govindaraj: Large aligned-nanotube bundles from ferrocene pyrolysis, *Chem. Commun.* **15**, 1525–1526 (1998)
- 7.45 R. Andrews, D. Jacques, A.M. Rao, F. Derbyshire, D. Qian, X. Fan, E.C. Dickey, J. Chen: Continuous production of aligned carbon nanotubes: a step closer to commercial realization, *Chem. Phys. Lett.* **303**, 467–474 (1999)
- 7.46 R. Kamalakaran, M. Terrones, T. Seeger, P. Kohler-Redlich, M. Ruhle, Y.A. Kim, T. Hayashi, M. Endo: Synthesis of thick and crystalline nanotube arrays by spray pyrolysis, *Appl. Phys. Lett.* **77**, 3385–3387 (2000)
- 7.47 M. Endo, Y.A. Kim, Y. Fukai, T. Hayashi, M. Terrones, H. Terrones, M.S. Dresselhaus: Comparison study of semi-crystalline and highly crystalline multiwalled carbon nanotubes, *Appl. Phys. Lett.* **79**, 1531–1533 (2001)
- 7.48 H. Terrones, T. Hayashi, M. Munoz-Navia, M. Terrones, Y.A. Kim, N. Grobert, R. Kamalakaran, J. Dorantes-Davila, R. Escudero, M.S. Dresselhaus, M. Endo: Graphitic cones in palladium catalysed carbon nanofibers, *Chem. Phys. Lett.* **343**, 241–250 (2001)
- 7.49 J.F. Despres, E. Daguerre, K. Lafdi: Flexibility of graphene layers in carbon nanotubes, *Carbon* **33**, 87–89 (1995)
- 7.50 M. Kosaka, T.W. Ebbesen, H. Hiura, K. Tanigaki: Annealing effect on carbon nanotubes. An ESR study, *Chem. Phys. Lett.* **233**, 47–51 (1995)
- 7.51 M. Endo, K. Nishimura, Y.A. Kim, K. Hakamada, T. Matsuhashita, M.S. Dresselhaus, G. Dresselhaus: Raman spectroscopic characterization of submicron vapor-grown carbon fibers and carbon nanofibers obtained by pyrolyzing hydrocarbons, *J. Mater. Res.* **14**, 4474–4477 (1999)
- 7.52 M. Endo, Y.A. Kim, T. Hayashi, T. Yanagisawa, H. Muramatsu, M. Ezaka, H. Terrones, M. Terrones, M.S. Dresselhaus: Microstructural changes induced in stacked cup carbon nanofibers by heat treatment, *Carbon* **41**, 1941–1947 (2003)
- 7.53 J. Campos-Delgado, H. Farhat, Y.A. Kim, A. Reina, J. Kong, M. Endo, H. Muramatsu, T. Hayashi, H. Terrones, M. Terrones, M.S. Dresselhaus: Resonant Raman study on bulk and isolated graphitic nanoribbons, *Small* **5**, 2698–2702 (2009)
- 7.54 G. Katagiri, H. Ishida, A. Ishitani: Raman spectra of graphite edge planes, *Carbon* **26**, 565–571 (1988)
- 7.55 M. Endo, T. Hayashi, S.H. Hong, T. Enoki, M.S. Dresselhaus: Scanning tunneling microscope study of boron-doped highly oriented pyrolytic graphite, *J. Appl. Phys.* **90**, 5670–5674 (2001)
- 7.56 P.G. Collins, M. Hersam, M. Arnold, R. Martel, P. Avouris: Current saturation and electrical breakdown in multiwalled carbon nanotubes, *Phys. Rev. Lett.* **86**, 3128–3131 (2001)
- 7.57 A.P. Graham, G.S. Duesberg, R.V. Seidel, M. Liebau, E. Unger, W. Pamler, F. Kreupl, W. Hoenlein: Carbon nanotubes for microelectronics?, *Small* **1**, 382–390 (2005)
- 7.58 B.Q. Wei, R. Vajtai, P.M. Ajayan: Reliability and current carrying capacity of carbon nanotubes, *Appl. Phys. Lett.* **79**, 1172–1174 (2001)
- 7.59 B.T. Kelly: *Physics of Graphite* (Springer, New York 1981)
- 7.60 N. Kurita, M. Endo: Molecular orbital calculations on electronic and Li-adsorption properties of sulfur-, phosphorus- and silicon-substituted disordered carbons, *Carbon* **40**, 253–260 (2002)
- 7.61 H. Jiang, C. Wu, A. Zhang, P. Yang: Structural characteristics of polyacrylonitrile (PAN) fibers during oxidative stabilization, *Compos. Sci. Technol.* **29**, 33–44 (1987)
- 7.62 H. Ogawa, K. Saito: Oxidation behavior of polyacrylonitrile fibers evaluated by new stabilization index, *Carbon* **33**, 783–788 (1995)

- 7.63 P.L. Walker: *Chemistry and Physics of Carbon* (Marcel Dekker, New York 1971)
- 7.64 R.J. Nemanichi, S.A. Solin: First- and second-order Raman scattering from finite-size crystals of graphite, *Phys. Rev. B* **20**, 392–401 (1970)
- 7.65 K. Kaneko, J. Imai: Adsorption of NO₂ on activated carbon fibers, *Carbon* **27**, 954–955 (1989)
- 7.66 S.H. Joo, S.J. Choi, I.W. Oh, J.Y. Kwak, Z. Liu, O. Terasaki, R. Ryoo: Ordered nanoporous arrays of carbon supporting high dispersions of platinum nanoparticles, *Nature* **412**, 169–172 (2001)
- 7.67 L. Schlapbach, A. Zettler: Hydrogen-storage materials for mobile applications, *Nature* **414**, 353–358 (2001)
- 7.68 M. Terrones: Science and technology of the twenty-first century: synthesis, properties, and applications of carbon nanotubes, *Annu. Rev. Mater. Res.* **33**, 419–501 (2003)
- 7.69 E. Belyarova, V. Murata, M. Yudasaka, D. Kasuya, S. Iijima, H. Tanaka, K. Kaneko: Single-wall nanostructured carbon for methane storage, *J. Phys. Chem. B* **107**, 4681–4684 (2003)
- 7.70 H. Take, T. Matsumoto, K. Yoshino: Anodic properties of porous carbon with periodic nanostructure, *Synth. Met.* **135–136**, 731–732 (2003)
- 7.71 R.C. Bansal, J.B. Donnet, H.F. Stoekli: *Active Carbon* (Marcel Dekker, New York 1988)
- 7.72 Z. Yang, Y. Xia, R. Mokaya: Zeolite ZSM-5 with unique supermicropores synthesized using mesoporous carbon as a template, *Adv. Mater.* **16**, 727–732 (2004)
- 7.73 J.W. Lee, S.J. Han, T.H. Hyeon: Synthesis of new nanoporous carbon materials using nanostructured silica materials as templates, *J. Mater. Chem.* **14**, 478–486 (2004)
- 7.74 A.B. Fuertes: A low-cost synthetic route to mesoporous carbons with narrow pore size distributions and tunable porosity through silica xerogel templates, *Chem. Mater.* **16**, 449–455 (2004)
- 7.75 J. Ozaki, N. Endo, W. Ohizumi, K. Igarashi, M. Nakahara, A. Oya: Novel preparation method for the production of mesoporous carbon fiber from a polymer blend, *Carbon* **35**, 1031–1033 (1997)
- 7.76 A. Oya, N. Kasahara: Preparation of thin carbon fibers from phenol-formaldehyde polymer microbeads dispersed in polyethylene matrix, *Carbon* **38**, 1141–1144 (2000)
- 7.77 D. Hulicova, F. Sato, K. Okabe, M. Koishi, A. Oya: An attempt to prepare carbon nanotubes by the spinning of microcapsules, *Carbon* **39**, 1438–1442 (2001)
- 7.78 Z.-M. Huang, Y.-Z. Zhang, M. Kotaki, S. Ramakrishna: A review on polymer nanofibers by electrospinning and their applications in nanocomposites, *Compos. Sci. Technol.* **63**, 2223–2253 (2003)
- 7.79 Y. Wang, S. Serrano, J.J. Santiago-Aviles: Conductivity measurement of electrospun PAN-based carbon nanofiber, *J. Mater. Sci. Lett.* **21**, 1055–1057 (2002)
- 7.80 Y. Wang, J.J. Santiago-Aviles, R. Furlan, I. Ramos: Pyrolysis temperature and time dependence of electrical conductivity evolution for electrostatically generated carbon nanofibers, *IEEE Trans. Nanotechnol.* **2**, 39–43 (2003)
- 7.81 Y. Wang, S. Serrano, J.J. Santiago-Aviles: Raman characterization of carbon nanofibers prepared using electrospinning, *Synth. Met.* **138**, 423–427 (2003)
- 7.82 S.Y. Gu, J. Ren, Q.L. Wu: Preparation and structures of electrospun PAN nanofibers as a precursor of carbon nanofibers, *Synth. Met.* **155**, 157–161 (2005)
- 7.83 S.Y. Gu, J. Ren, G.J. Vancso: Process optimization and empirical modeling for electrospun polyacrylonitrile (PAN) nanofiber precursor of carbon nanofibers, *Eur. Polym. J.* **41**, 2559–2568 (2005)
- 7.84 D. Lai, Y. Xia: Electrospinning of nanofibers: reinventing the wheel, *Adv. Mater.* **16**, 1151–1170 (2004)
- 7.85 D. Hulicova, K. Hosoi, S. Kuroda, H. Abe, A. Oya: Carbon nanotubes prepared by spinning and carbonizing fine core-shell polymer microspheres, *Adv. Mater.* **14**, 452–455 (2002)
- 7.86 E. Zussman, A.L. Yarin, A.V. Brazilevsky, R. Avrahami, M. Feldman: Electrospun PAN/PMMA-derived carbon nanotubes, *Adv. Mater.* **18**, 348–353 (2006)
- 7.87 J. Brandrup, E.H. Immergut, E.A. Grulke, D. Bloch: *Polymer Handbook* (Wiley, New York 2005)
- 7.88 M. Winter, J.O. Besenhard, M.E. Spahar, P. Novak: Electrode materials for rechargeable lithium batteries, *Adv. Mater.* **10**, 725–763 (1998)
- 7.89 T.D. Burchell: *Carbon Materials for Advanced Technologies* (Elsevier, Amsterdam 1999)
- 7.90 M. Endo, C. Kim, K. Nishimura, T. Fujino, K. Miyashita: Recent development of carbon materials for Li ion batteries, *Carbon* **38**, 183–197 (2000)
- 7.91 E. Frackowiak, F. Beguin: Electrochemical storage of energy in carbon nanotubes and nanostructured carbons, *Carbon* **40**, 1775–1787 (2002)
- 7.92 E. Yasuda, M. Inagaki, K. Kaneko, M. Endo, A. Oya, Y. Tanabe: *Carbon Alloy* (Elsevier, Amsterdam 2003)
- 7.93 V.A. Alimova, D.E. Sklovsky, G.N. Bondarenko, H. Alvergnat-Gaucher, S. Bonnamy, F. Beguin: Lithium interaction with carbon nanotubes, *Synth. Met.* **88**, 89–93 (1997)
- 7.94 B. Gao, A. Kleinhanns, X.P. Tang, C. Bower, L. Fleming, Y. Wu, O. Zhou: Electrochemical intercalation of single-walled carbon nanotubes with lithium, *Chem. Phys. Lett.* **307**, 153–157 (1999)
- 7.95 F. Leroux, K. Metenier, S. Gautier, E. Frackowiak, S. Bonnamy, F. Beguin: Electrochemical insertion of lithium in catalytic multi-walled carbon nanotubes, *J. Power Source* **81–82**, 317–322 (1999)
- 7.96 A.S. Claye, J.E. Fischer, C.B. Huffman, A.G. Rinzler, R.E. Smalley: Solid-state electrochemistry of the Li single wall carbon nanotube system, *J. Electrochem. Soc.* **147**, 2845–2852 (2000)
- 7.97 R.S. Morris, B.G. Dixon, T. Gennett, R. Raffaelle, M.J. Heben: High-energy, rechargeable Li-ion battery based on carbon nanotube technology, *J. Power Source* **138**, 277–280 (2004)
- 7.98 G.L. Che, B.B. Lakshmi, E.R. Fisher, C.R. Martin: Carbon nanotubule membranes for electrochemical

- energy storage and production, *Nature* **393**, 346–349 (1998)
- 7.99 M. Endo, Y.A. Kim, T. Hayashi, K. Nishimura, T. Matushita, K. Miyashita, M.S. Dresselhaus: Vapor-grown carbon fibers (VGCFs): Basic properties and their battery applications, *Carbon* **39**, 1287–1297 (2001)
- 7.100 C. Sotowa, G. Origi, M. Takeuchi, Y. Nishimura, K. Takeuchi, I.Y. Jang, Y.J. Kim, T. Hayashi, Y.A. Kim, M. Endo, M.S. Dresselhaus: The reinforcing effect of combined carbon nanotubes and acetylene blacks on the cathode electrode of lithium ion batteries, *ChemSusChem* **1**, 911–915 (2008)
- 7.101 F. Fong, K. Sacken, J.R. Dahn: Studies of lithium intercalation into carbons using nonaqueous electrochemical cells, *J. Electrochim. Soc.* **137**, 2009–2013 (1990)
- 7.102 S.H. Yoon, C.W. Park, H.J. Yang, Y. Korai, I. Mochida, R.T.K. Baker, N.M. Rodriguez: Novel carbon nanofibers of high graphitization as anodic materials for lithium ion secondary batteries, *Carbon* **42**, 21–32 (2004)
- 7.103 T. Doi, A. Fukuda, Y. Iriyama, T. Abe, Z. Ogumi, K. Nakagawa, T. Ando: Low-temperature synthesis of graphitized nanofibers for reversible lithium-ion insertion/extraction, *Electrochim. Commun.* **7**, 10–13 (2005)
- 7.104 J.K. Lee, K.W. An, J.B. Ju, B.W. Cho, W.I. Cho, D. Park, K.S. Yun: Electrochemical properties of PAN-based carbon fibers as anodes for rechargeable lithium ion batteries, *Carbon* **39**, 1299–1305 (2001)
- 7.105 B.E. Conway: *Electrochemical Supercapacitors—Scientific Fundamentals and Technological Applications* (Kluwer, New York 1999)
- 7.106 A.G. Pandolfo, A.F. Hollenkamp: Carbon properties and their role in supercapacitors, *J. Power Source* **157**, 11–27 (2006)
- 7.107 A. Yoshida, I. Tanahashi, A. Nishino: Effect of concentration of surface acidic functional groups on electric double-layer properties of activated carbon fibers, *Carbon* **28**, 611–615 (1990)
- 7.108 A. Nishino: Capacitors: operating principles, current market and technical trends, *J. Power Source* **60**, 137–147 (1990)
- 7.109 J.P. Zheng: Ruthenium oxide–carbon composite electrodes for electrochemical capacitors, *Electrochim. Solid-State Lett.* **2**, 359–361 (1999)
- 7.110 E. Frackowiak, F. Béguin: Carbon materials for the electrochemical storage of energy in capacitors, *Carbon* **39**, 937–950 (2001)
- 7.111 M. Endo, T. Maeda, T. Takeda, Y.J. Kim, K. Koshiba, H. Hara, M.S. Dresselhaus: Capacitance and pore-size distribution in aqueous and nonaqueous electrolytes using various activated carbon electrodes, *J. Electrochim. Soc.* **148**, A910–A914 (2001)
- 7.112 C. Niu, E.K. Sichel, R. Hoch, D. Moy, H. Tennent: High power electrochemical capacitors based on carbon nanotube electrodes, *Appl. Phys. Lett.* **70**, 1480–1482 (1997)
- 7.113 C.Y. Liu, A.J. Bard, F. Wudl, I. Weitz, J.R. Heath: Electrochemical characterization of films of single-walled carbon nanotubes and their possible application in supercapacitors, *Electrochim. Solid State Lett.* **2**, 577–578 (1999)
- 7.114 E. Frackowiak, K. Metenier, V. Bertagna, F. Béguin: Supercapacitor electrodes from multiwalled carbon nanotubes, *Appl. Phys. Lett.* **77**, 2421–2423 (2000)
- 7.115 K.H. An, W.S. Kim, Y.S. Park, Y.C. Choi, S.M. Lee, D.C. Chung, D.J. Bae, S.C. Lim, Y.H. Lee: Supercapacitors using single-walled carbon nanotube electrodes, *Adv. Mater.* **13**, 497–500 (2001)
- 7.116 E. Frackowiak, F. Béguin: Electrochemical storage of energy in carbon nanotubes and nanostructured carbons, *Carbon* **40**, 1775–1787 (2002)
- 7.117 Z. Yie, C.L. Mangun, J. Economy: Preparation of fibrous porous materials by chemical activation: 1. $ZnCl_2$ activation of polymer-coated fibers, *Carbon* **40**, 1181–1191 (2002)
- 7.118 N. Yalcin, V. Sevinc: Studies of the surface area and porosity of activated carbons prepared from rice husks, *Carbon* **38**, 1943–1945 (2000)
- 7.119 A. Huidobro, A.C. Pastor, F. Rodriguez-Reinoso: Preparation of activated carbon cloth from viscous rayon: Part IV. Chemical activation, *Carbon* **39**, 389–398 (2001)
- 7.120 J.M. Planeix, N. Coustel, B. Coq, V. Brotons, P.S. Kumbhar, R. Dutartre: Application of carbon nanotubes as supports in heterogeneous catalysis, *J. Am. Chem. Soc.* **116**, 7935–7936 (1994)
- 7.121 W. Li, C. Liang, J. Qiu, W. Zhou, H. Han, Z. Wei, G. Sun, Q. Xin: Carbon nanotubes as support for cathode catalyst of a direct methanol fuel cell, *Carbon* **40**, 791–794 (2002)
- 7.122 H.C. Choi, M. Shim, S. Bangsaruntip, H. Dai: Spontaneous reduction of metal ions on the sidewalls of carbon nanotubes, *J. Am. Chem. Soc.* **124**, 9058–9059 (2002)
- 7.123 L.R. Radovic, F. Rodriguez-Reinoso: Carbon materials in catalysis, *Chem. Phys. Carbon* **25**, 243–358 (1997)
- 7.124 M.C. Roman-Martinez, D. Cazorla-Amoros, A. Linare-Solano, C. Salinas-Martinez De Lecea, H. Yamashita, M. Anpo: Metal–support interaction in Pt/C catalysts. Influence of the support surface chemistry and the metal precursor, *Carbon* **33**, 3–13 (1995)
- 7.125 M. Endo, Y.A. Kim, M. Ezaka, K. Osada, T. Yanagisawa, T. Hayashi, M. Terrones, M.S. Dresselhaus: Selective and efficient impregnation of metal nanoparticles on cup-stacked-type nanofibers, *Nano Lett.* **3**, 723–726 (2003)
- 7.126 C. Kim, Y.A. Kim, J.H. Kim, M. Kataoka, M. Endo: Self-assembled palladium nanoparticles on carbon nanofibers, *Nanotechnology* **19**, 145602 (2008)
- 7.127 K.A. Faraj, T.H. van Kuppevelt, W.F. Daamen: Construction of collagen scaffolds that mimic the

- three-dimensional architecture of specific tissues, *Tissue Eng.* **13**, 2387–2394 (2007)
- 7.128 M.T. Valarmathi, M.J. Yost, R.L. Goodwin, J.D. Potts: The influence of proepicardial cells on the osteogenic potential of marrow stromal cells in a three-dimensional tubular scaffold, *Biomaterials* **29**, 2203–2216 (2008)
- 7.129 J. Glowacki, S. Mizuno: Collagen scaffolds for tissue engineering, *Biopolymers* **89**, 338–344 (2008)
- 7.130 A. Atala, S.B. Bauer, S. Soker, J.J. Yoo, A.B. Retik: Tissue-engineered autologous bladders for patients needing cystoplasty, *Lancet* **367**, 1241–1246 (2006)
- 7.131 J.C. Chachques, J.C. Trainini, N. Lago, O.H. Mansoli, J.L. Barisani, M. Cortes-Morichetti, O. Schussler, A. Carpentier: Myocardial assistance by grafting a new bioartificial upgraded myocardium (MAGNUM clinical trial): one year follow-up, *Cell Transplant.* **16**, 927–934 (2007)
- 7.132 F. DeLustro, J. Dasch, J. Keefe, L. Ellingsworth: Immune responses to allogeneic and xenogeneic implants of collagen and collagen derivatives, *Clin. Orthop. Relat. Res.* **260**, 263–279 (1990)
- 7.133 D. Butler: Last chance to stop and think on risks of xenotransplants, *Nature* **391**, 320–324 (1998)
- 7.134 F.H. Bach, J.A. Fishman, N. Daniels, J. Proimos, B. Anderson, C.B. Carpenter, L. Forrow, S.C. Robson, H.V. Fineberg: Uncertainty in xenotransplantation: individual benefit versus collective risk, *Nat. Med.* **4**, 141–144 (1998)
- 7.135 J.R. Parsons, A.B. Weiss, R.S. Schenk, H. Alexander, F. Pavlisko: Long-term follow-up of achilles tendon repair with an absorbable polymer carbon fiber composite, *Foot Ankle.* **9**, 179–184 (1989)
- 7.136 T. Visuri, O. Kiviluoto, M. Eskelin: Carbon fiber for repair of the rotator cuff. A 4-year follow-up of 14 cases, *Acta Orthop. Scand.* **62**, 356–359 (1991)